



Ellipsoidal soft micro-particles suspended in dilute viscous flow

Jana Wedel ^a^{*}, Matjaž Hriberšek ^b, Jure Ravnik ^b¹, Paul Steinmann ^{a,c}

^a Institute of Applied Mechanics, Universität Erlangen-Nürnberg, Germany

^b Faculty of Mechanical Engineering, University of Maribor, Slovenia

^c Glasgow Computational Engineering Center, University of Glasgow, United Kingdom

ARTICLE INFO

Keywords:

Soft particles
Lagrangian particle tracking
Pseudo-rigid bodies
Point-particle method

ABSTRACT

Soft particles in viscous flows are prevalent both in nature and in various industrial applications. Notable examples include biological cells such as blood cells and bacteria as well as hydrogels and vesicles. To model these intriguing particles, we present an extension of our recent, efficient, and versatile pseudo-rigid body approach, originally developed for initially spherical soft particles suspended in arbitrary macroscale viscous flows. The novel extension allows modeling the barycenter and shape dynamics of soft initially non-spherical, i.e. ellipsoidal particles by introducing a novel shape and orientation tensor. We consider soft, micrometer-sized, ellipsoidal particles deforming affinely. To this end, we combine affine deformations (as inherent to a pseudo-rigid body) and the Jeffery-Roscoe model to analytically determine the traction exerted on a soft ellipsoidal particle suspended locally in a creeping flow at the particle scale. Without loss of generality, we assume nonlinear hyperelastic material behavior for the particles considered. The novel extension of our recent numerical approach for soft particles demonstrates that the deformation and motion of the particles can be accurately reproduced also for ellipsoidal particles and captures results from the literature, however, at drastically reduced computational costs. Furthermore, we identify both the tumbling and trembling dynamic regime for soft ellipsoidal particles suspended in simple shear flow again capturing results from the literature. Our extended approach is first validated using experimental and numerical studies from the literature for quasi-rigid as well as soft particles, followed by a comparison of the effects of particle deformability for some well-known fluid flow cases, such as laminar pipe flow, lid-driven cavity flow, and a simplified bifurcation. We find that taking particle deformability into account leads to notable deviations in the particle trajectory compared to rigid particles, with increased deviations for higher initial particle aspect ratio. Furthermore, we demonstrate that our approach can track a statistically relevant number of soft particles in complex flow situations.

1. Introduction

Particles in flows are widely present in nature, from platelets in the blood to asbestos fibers in the air to microplastics in the oceans. In addition, various industries rely on handling particulate systems suspended in fluids, especially in petrochemical, wastewater, cement, or pharmaceutical industries, [1,2]. The research on suspension of rigid particles is vast, see several analytical [3–7], experimental [8–12], and computational [13–20] studies for spherical and non-spherical rigid particles. However, rigidity of the suspended particles is not always given and thus, a particle might change shape due to the action of the surrounding fluid. Even

* Corresponding author.

E-mail address: jana.wedel@fau.de (J. Wedel).

<https://doi.org/10.1016/j.cma.2025.117973>

Received 11 December 2024; Received in revised form 20 March 2025; Accepted 25 March 2025

Available online 18 April 2025

0045-7825/© 2025 Published by Elsevier B.V.

though there exist pertinent examples of soft particles, i.e. both man-made (liposomes, vesicles, hydrogels, liquid capsules, [21], filled polymers [22]) and naturally occurring (biological cells, [23], bacteria, algae), only limited research is available, [24], especially when large numbers of particles are involved, and as a consequence, the knowledge about these systems remains limited.

1.1. State-of-the-art on modeling soft micro-particles in flows

Pioneering research on soft particles was conducted by Fröhlich and Sack, [25], who studied Hookean elastic particles of initially spherical shape suspended in extensional Newtonian flow. Cerf, [26], studied an infinite dilute suspension of viscoelastic spheres in a viscous fluid experiencing small amplitude oscillatory motion. Later, Goddard & Miller, [27], investigated the transient shape dynamics of visco-elastic spheres that were slightly deformable and surrounded by a Newtonian fluid under Stokes flow conditions. As stated by Sanagavarapu, [21] the above prominent studies [25–27] on deformable elastic (and viscoelastic) particles suspended in flows are targeting the small deformation regime, i.e. assuming a simplifying linear constitutive relation for the elastic stress.

Roscoe, [28], was the first to study suspensions of visco-elastic micro-particles of initially spherical shape suspended in viscous flows targeting the regime of finite and large deformations. Note that Roscoe's work serves as an extension to the seminal work of Jeffery, [7], who studied rigid ellipsoids, and the work of Cerf, [26]. Roscoe observed that the considered particles (of initially spherical shape) suspended in simple shear flow adopt, after a transient stage, a stationary ellipsoidal shape with a fixed orientation. However, the material points within the ellipsoids undergo continuous deformation, i.e. the so-called tank-treading motion, [28]. Roscoe's underlying assumption of affine deformation was validated first in 2D (initially circular particles) by Gao & Hue, [29], and later in 3D (initially spherical particles) by Gao et al. [30]. The authors observed in their numerical simulations the predicted steady-state ellipsoidal shape and orientation as well as the tank-treading phenomenon in their research. Note that the theoretical framework of Gao et al. for describing the particle deformation bases on a polarization technique and requires a surface discretization. Later, Gao et al. [31], extended the theoretical framework to include prolate ellipsoidal soft particles suspended in planar shear flow. The authors observed that the ellipsoidal particles experience either a tumbling behavior as in the quasi-rigid particle limit or a so-called trembling regime, which was also experimentally observed in vesicles, [31]. Furthermore, Gao et al. [32], investigated 2D elliptic particles in extensional flow and observed that the steady-state particle shape (long axis of the particle aligned with the extensional direction of the flow) varies from the steady-state shape of a similar particle suspended in a shear flow. As pointed out by Sanagavarapu et al. [21], the theoretical framework of Gao et al. [29–32], to model soft particles in flows, bases on the upper convective time derivative of the Neo-Hooke constitutive relation to obtain the stress rate versus strain rate relationship. However, Sanagavarapu et al. [21], states that this is a restricting factor of the framework as it cannot be employed for general constitutive relations such as, e.g., the Mooney–Rivlin constitutive model, as here the stress rate cannot be related to strain rate alone. As an improvement, Sanagavarapu et al. [21], suggest directly relating the total stress to the total strain, i.e. the conventional approach in hyperelasticity. Note that similar to the work of Gao et al. [29–32], the work of Sanagavarapu et al. [21], requires a particle discretization to capture the particle deformability and thus both frameworks are clearly limited by the number of soft particles that can be considered simultaneously.

Taken together, we note that the frameworks proposed in the literature targeting either analytical and/or computational solutions focused mainly on initially spherical or, with some exceptions, on initially ellipsoidal soft particles under restrictive assumptions. These assumptions arise from the derivation for either a specific constitutive behavior of the soft particles and/or flow conditions. Note that in addition to these restrictions, the available computational frameworks require particle discretization and thus typically require significant computational cost, especially when large numbers of particles have to be considered.

In our recent work, see Wedel et al. [33], we presented a novel, efficient, and utmost versatile model for tracking large numbers ($\geq \mathcal{O}(10^5)$) of initially spherical soft particles suspended in arbitrary flow conditions, by assuming affine transformation and arbitrary hyperelastic material behavior in combination with the point-particle approach. A detailed discussion on the efficiency of the novel model is presented in Appendix F of [33].

Note that in our previous work, see Wedel et al. [33], we employ the heretofore mostly overlooked pseudo-rigid body theory, as advocated by Cohen & Munchaster [34], as it perfectly matches the kinematic conditions of soft ellipsoidal micro-particles suspended in viscous flows. Without loss of generality, we presented our framework using a Neo-Hookean constitutive law. Due to its versatility, this model is the ideal launching pad to model more complex behaviors. Thus, in this work, we extend our framework to model initially non-spherical, i.e. ellipsoidal soft particles.

1.2. Pseudo-rigid body approach for soft micro-particles in dilute flows

As stated above, we employ the heretofore mostly overlooked pseudo-rigid body theory, [34], in combination with the point-particle approach with Lagrangian particle tracking. Recall that in general, pseudo-rigid bodies are characterized by affine deformation and thus can be interpreted as a first-order extension to the kinematics of rigid bodies. Employing state-of-the-art computational solution of the Navier–Stokes equations in combination with the point-particle approach (particle surface and bulk is not discretized) enables comparatively low costs in tracking, [35], of a realistically large number ($\geq \mathcal{O}(10^5)$) of particles suspended in arbitrary flow fields. Note that this is in strong contrast to the methods otherwise available in the soft particle literature, which rely on particle discretization and thus are strongly limited with respect to the number of particles that can be considered simultaneously.

To track soft particles of ellipsoidal shape dilutely dispersed in arbitrary flow fields, we employ a global–local, i.e. two-scale framework. The decomposition into global and local scales is possible, as we assume a one-way coupling, and thus the flow-field is updated independently of the particulate phase. The *global problem at the macro-scale* is identical to our recent approach (see Wedel

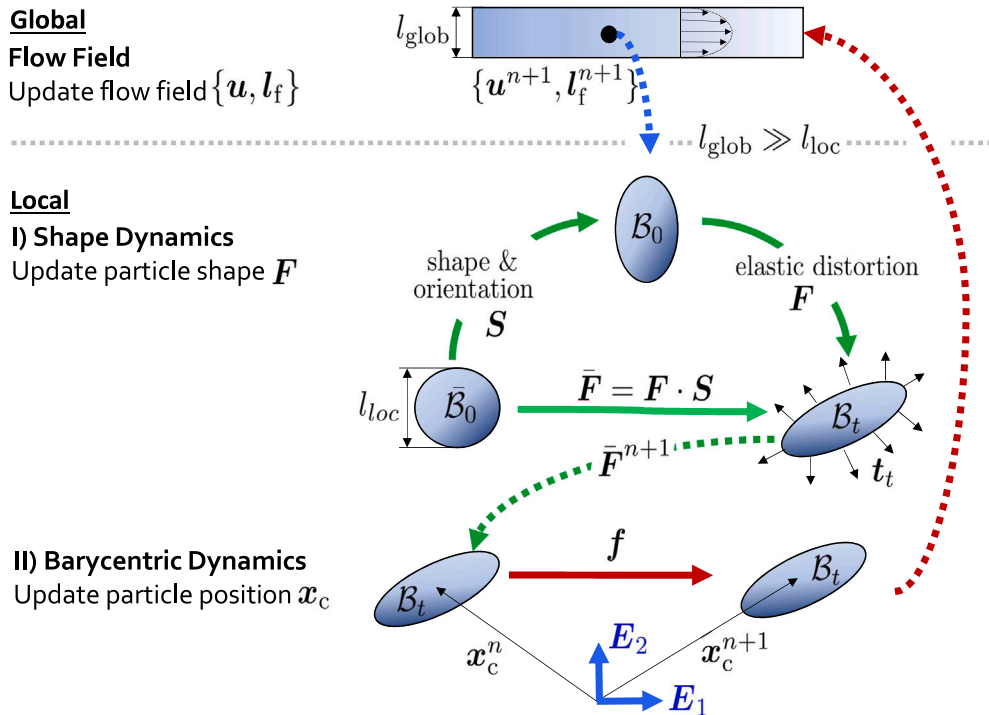


Fig. 1. Sketch of the novel pseudo-rigid body approach to the non-linear dynamics of soft micro-particles in viscous flow. Tracking soft micro-particles in flows is treated as a global–local, i.e. two-scale problem. In the macro-scale problem (global characteristic length l_{glob}) we solve for the flow field without accounting for the particle phase, i.e. one-way coupling approach. Then, the flow velocity u^{n+1} and the velocity gradient l_f^{n+1} at the current particle center x_c are obtained. On the micro-scale (local characteristic length l_{loc} with $l_{loc} \ll l_{glob}$) there are two separate problems. The first is denoted as shape dynamics and consists of finding the distortion F^{n+1} to obtain the new particle shape, i.e. $\bar{F}^{n+1} = F^{n+1} \cdot S$ with S the shape and orientation tensor. Given the new particle shape (\bar{F}^{n+1}), we can solve the second local problem, i.e. the barycentric dynamics, where we update the particle position x_c using established force models f according to Brenner, [36]. In the next time step, we first update the flow field (neglecting the particle influence on the fluid, since we consider one-way coupling). Next we can identify the new flow velocity u^{n+1} and the velocity gradient l_f^{n+1} at the particle position x_c^{n+1} , which are required inputs for the shape and barycentric dynamics.

et al. [33]). Here, we update the fluid flow quantities at a given time step in the flow field (macro-scale) independently of the soft particles. The *local problem* is at the micro-scale and can be decomposed in two subsequent problems. We denote the *first problem at the micro-scale* the shape problem. Here, we first define the initial ellipsoidal shape and orientation B_0 from a reference sphere \bar{B}_0 and a shape and orientation tensor S . Next, we compute the deformed particle shape B_t for the given initial ellipsoidal shape B_0 and for given tractions t_t exerted by the fluid flow on the particle, see Fig. 1. After obtaining the deformed particle shape B_t at the current time step, we proceed with the second *local problem at the micro-scale*, which consists of computing the particle's time-discrete barycenter trajectory using established force models for the deformed particle shape B_t . We want to highlight that at the local scale, the Reynolds numbers are typically well below one, thus we safely assume local Stokes flow around the suspended particles.

The notation in this work is based on our previous work, see [33], for convenience, it is recapitulated in Appendix. Furthermore, in order to simplify the notation as much as possible, we only use super- or subscripts $(\bullet)^s$, $(\bullet)_s$ and $(\bullet)^f, (\bullet)_f$ indicating whether a property (superscript) or kinematic quantity (subscript) (\bullet) refers to the solid or the fluid embedding it if there is otherwise a risk of confusion.

2. Pseudo-rigid body dynamics

To set the stage, we briefly recall the dynamics of pseudo-rigid bodies as proposed by Cohen and Muncaster [34].

2.1. Kinematics of a pseudo-rigid body

Let a solid continuum body consisting of physical points P be denoted as $B = \{P\}$, with the reference configuration \bar{B}_0 (here a unit sphere), the material configuration B_0 (stress-free) and the spatial configuration B_t (deformed). Note that the spatial positions

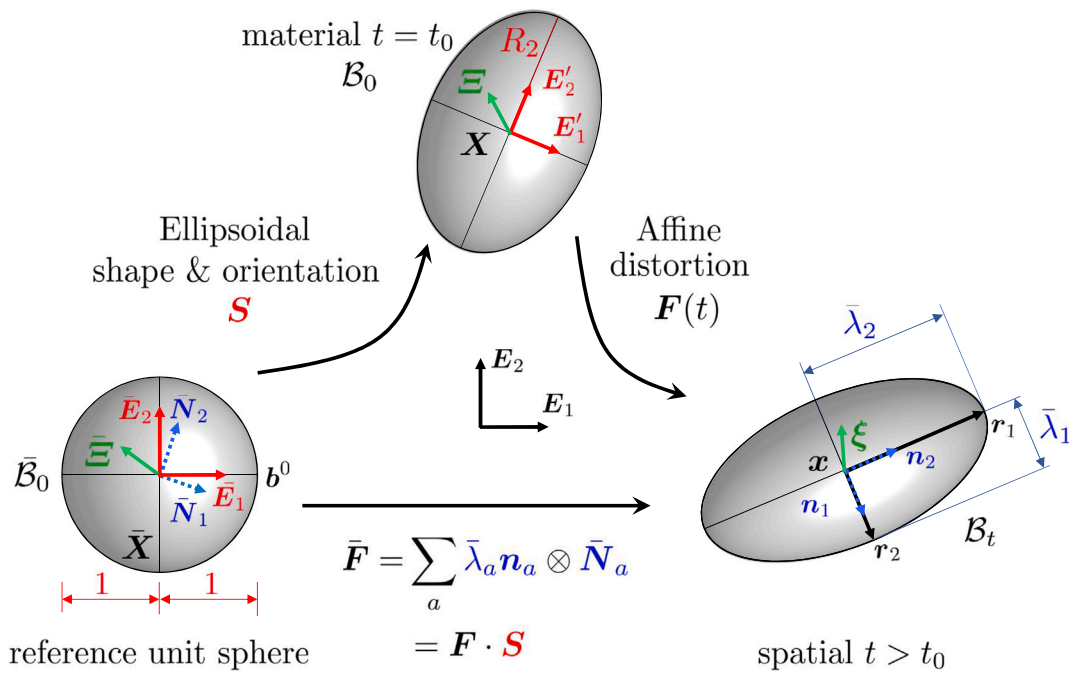


Fig. 2. Example of a pseudo-rigid body: Affine deformation of an ellipsoid into an ellipsoid. Notation: Initial ellipsoid (material configuration) with half axes R_a deforming into an ellipsoid with half axes r_a with $a = 1, 2, 3$; Relative reference, material and spatial positions $\bar{\Xi}$, Ξ and ξ connecting the barycenter with the reference, material and spatial positions \bar{X} in the reference configuration \bar{B}_0 , X in the material configuration B_0 and x in the spatial configuration B_t , respectively, of a pseudo-rigid body; Lagrangian principal directions \bar{N}_a in the reference configuration \bar{B}_0 and Eulerian principal directions n_a in the spatial configuration B_t with $a = 1, 2, 3$. Fixed inertial frame of reference E_a with $a = 1, 2, 3$ (iFoR).

$x \in B_t$ of the physical points P are obtained by applying the deformation map $x = \bar{y}(t, \bar{X})$, i.e. a nonlinear vector-valued function of time and space, to the reference positions $\bar{X} \in \bar{B}_0$ of the physical points P . Furthermore, let $\bar{\rho}_0^s$, ρ_0^s and ρ_t^s denote the mass density (of the solid material) per unit volume in \bar{B}_0 (a scalar-valued function of \bar{X}), per unit volume in B_0 (a scalar-valued function of X) and per unit volume in B_t (a scalar-valued function of x), respectively.

Fig. 2 sketches the affine deformation of an ellipsoid in the stress-free material configuration B_0 into a deformed ellipsoid in the spatial configuration B_t by using a reference unit sphere in the reference configuration \bar{B}_0 in combination with a shape and orientation tensor S .

The material positions X of a pseudo-rigid body expand as

$$X = X_c + \Xi \quad \text{with} \quad \Xi := X - X_c \quad \text{and the barycenter condition} \quad \int_{B_0} \rho_0^s \Xi \, dV \equiv \mathbf{0}, \tag{1}$$

where X_c denotes the material position of its barycenter, Ξ the relative material position and dV the material volume element. Followingly, the deformation map $y(t, X)$ of a pseudo-rigid body is a superposition of its barycenter motion $x_c = y_c(t)$ and its shape change $\xi(t, \Xi)$ and expands as

$$x = y(t, X) = y_c(t) + \xi(t, \Xi) \quad \text{with} \quad X_c = y_c(t=0) \quad \text{and} \quad \xi := F(t) \cdot \Xi \quad \text{with} \quad \mathbf{1} = F(t=0), \tag{2}$$

where the shape change $\xi(t, \Xi)$ is an affine deformation depending on the spatially uniform deformation gradient $F(t)$ and the relative material positions Ξ , whereby $\mathbf{1}$ denotes the (two-point) unit tensor.

The spatial volume element is obtained using the Jacobian $J := \det F > 0$ of the deformation gradient as $dv = J \, dV$ which can be likewise applied to the relation of the total volumes occupied by the pseudo-rigid body in the spatial ($\text{vol}(B_t)$) and material ($\text{vol}(B_0)$) configuration, i.e. $\text{vol}(B_t) = J \, \text{vol}(B_0)$, as J is spatially uniform. To describe the velocities of the physical points P of the pseudo-rigid body, we evaluate the material time derivative (at fixed X) of the deformation map which expands as

$$v := v_c(t) + v(t, \Xi) \quad \text{with} \quad v_c := \dot{y}_c(t) \quad \text{and} \quad v := \dot{\xi}(t, \Xi) = \dot{F}(t) \cdot \Xi =: A(t) \cdot \Xi. \tag{3}$$

Observe that we abbreviate the material velocity gradient \dot{F} as $A := \dot{F}$. The deformation map of the unit sphere to the material configuration consists only of an affine shape change contribution $\Xi(\bar{\Xi})$ and thus expands as

$$\Xi := S \cdot \bar{\Xi} \quad \text{with} \quad S := \sum_a R_a E'_a \otimes \bar{E}_a, \tag{4}$$

where R_a denote the semi-axis of the initially stress-free ellipsoidal particle in B_0 . Inserting $\Xi := S \cdot \bar{\Xi}$ in Eq. (2), the deformation map of the unit sphere to the spatial configuration expands as

$$\mathbf{x} = \mathbf{y}_c(t) + [\mathbf{F}(t) \cdot \mathbf{S}] \cdot \bar{\Xi}. \quad (5)$$

2.2. Barycenter dynamics

The Euler–Lagrange equation governing the barycenter dynamics of a pseudo-rigid body results as

$$\dot{\mathbf{v}}_c m = \mathbf{f} \quad \text{with} \quad \mathbf{f} := \int_{B_0} \mathbf{b}_0 dV + \int_{\partial B_0} \mathbf{t}_0 dA \quad (6)$$

with \mathbf{f} denoting the resultant of the conservative bulk and surface force densities \mathbf{b}_0 and \mathbf{t}_0 , respectively.

2.3. Shape dynamics

The Euler–Lagrange equation governing the shape dynamics of a pseudo-rigid body expands as

$$\dot{\mathbf{A}} \cdot \boldsymbol{\Theta} + \mathbf{P} \text{vol}(B_0) = \mathbf{M} \quad \text{with} \quad \mathbf{M} := \int_{B_0} \mathbf{b}_0 \otimes \Xi dV + \int_{\partial B_0} \mathbf{t}_0 \otimes \Xi dA. \quad (7)$$

where the right-hand side denotes the corresponding force dyad \mathbf{M} (resultant of the dyadic moment of the bulk and surface force densities with Ξ) and \mathbf{P} the Piola stress.

In addition, we define the total mass m and the material Euler tensor $\boldsymbol{\Theta}$ of the pseudo-rigid body as

$$m := \int_{B_0} \rho_0^s dV \quad \text{and} \quad \boldsymbol{\Theta} := \int_{B_0} \rho_0^s \Xi \otimes \Xi dV. \quad (8)$$

2.4. Constitutive behavior

Without loss of generality, we will assume in the following a quasi-incompressible Neo-Hooke stored energy density $w_0 = w_0(\mathbf{F})$, resulting in the Piola stress $\mathbf{P} = \partial w_0 / \partial \mathbf{F}$ expanding as

$$\mathbf{P} = \mu^s [\mathbf{F} - \mathbf{F}^{-t}] + \lambda^s \ln J \mathbf{F}^{-t}. \quad (9)$$

Here, λ^s and μ^s denote the first and second Lamé parameter respectively with $\lambda^s \rightarrow \infty$ describing the incompressible limit. The transition from the pseudo-rigid body shape dynamics equation to the common equations of motion of a rigid body are detailed in our previous work, see [33].

3. Resultant loading on a pseudo-rigid body of ellipsoidal shape

For spatially uniform mass-specific bulk force density \mathbf{a} (with the dimension of an acceleration) the corresponding contribution to \mathbf{f} simplifies to $\mathbf{a} m$. Observe that the traction $\mathbf{t}_0 = \bar{\mathbf{t}}_0 + \tilde{\mathbf{t}}_0$ can be decomposed into a constant vector $\bar{\mathbf{t}}_0$ (its surface average), and a fluctuation contribution

$$\bar{\mathbf{t}}_0 := \frac{1}{\text{sur}(\partial B_0)} \int_{\partial B_0} \mathbf{t}_0 dA \quad \text{and} \quad \mathbf{0} \equiv \int_{\partial B_0} \tilde{\mathbf{t}}_0 dA, \quad (10)$$

with $\text{sur}(\partial B_0)$ denoting the surface area of the pseudo-rigid body in its material configuration. By integrating over the particle surface, the fluctuation contribution vanishes, [33], and the corresponding contribution to \mathbf{f} thus simplifies to $\bar{\mathbf{t}}_0 \text{sur}(\partial B_0)$, here captured by the Brenner drag force. Furthermore, the contribution of the traction \mathbf{t}_0 to the force dyad \mathbf{M} depends on its fluctuation $\tilde{\mathbf{t}}_0$ only, that is

$$\mathbf{M} = \int_{\partial B_0} \tilde{\mathbf{t}}_0 \otimes \Xi dA. \quad (11)$$

3.1. Jeffery–Roscoe traction

Following, our previous work, see [33], a spatially uniform (constant) Cauchy-type stress $\bar{\boldsymbol{\sigma}}$ can be obtained analytically from the Roscoe–Jeffery traction ($\bar{\mathbf{i}}_t = \bar{\boldsymbol{\sigma}} \cdot \mathbf{n}$) expressions for an ellipsoidal body immersed in Stokes flow and reads as

$$\bar{\boldsymbol{\sigma}} = -\bar{p}(\mathbf{d}) \mathbf{i} + \mu^f [\bar{\mathfrak{s}}(\mathbf{d}, \mathbf{w}) + 2 \mathbf{d}_s]. \quad (12)$$

Here, \bar{p} and $\bar{\mathfrak{s}}$ are a spatially constant factor and a spatially constant (non-symmetric) and deviatoric second-order tensor, (both depending on the current ellipsoid shape in the spatial configuration), respectively. Furthermore, $\mathbf{d} := \mathbf{d}_f - \mathbf{d}_s$ denotes the modified rate of deformation tensor and $\mathbf{w} := \mathbf{w}_f - \mathbf{w}_s$ the modified spin (vorticity tensor). Note that $\mathbf{d}_s := \mathbf{l}_s^{\text{sym}}$ and $\mathbf{w}_s := \mathbf{l}_s^{\text{skw}}$ (with $\mathbf{l}_s := \mathbf{A} \cdot \mathbf{F}^{-1}$ the spatial velocity gradient of the solid) denote the deformation tensor and the vorticity tensor of the solid, respectively. Furthermore, $\mathbf{d}_f := \mathbf{l}_f^{\text{sym}}$ and $\mathbf{w}_f := \mathbf{l}_f^{\text{skw}}$ denote the deformation tensor and the vorticity tensor of the fluid, respectively. The terms $\bar{p}(\mathbf{d})$ and $\bar{\mathfrak{s}}(\mathbf{d}, \mathbf{w})$ can be evaluated in a similar fashion as proposed by Jeffery [7], and are detailed in our previous work [33].

3.2. Resultant force

In consistency with our previous work, we assume a locally small Stokes number, i.e. $St \ll 1$, around the particle, and thus the resultant force \mathbf{f} exerted on an ellipsoid in a viscous fluid is the reduced gravity force (reduced by buoyancy) \mathbf{f}_G as well as the drag force \mathbf{f}_D , i.e. $\mathbf{f} = \mathbf{f}_G + \mathbf{f}_D$. The reduced gravity force (reduced by buoyancy) reads as

$$\mathbf{f}_G = \mathbf{a}_G m = [\rho_i^s - \rho^f] \mathbf{g} \text{vol}(B_t) \text{ with } m = \rho_i^s \text{vol}(B_t), \quad (13)$$

while the drag force (\mathbf{f}_D) model by Brenner, [36], applicable for arbitrarily shaped bodies expands as

$$\mathbf{f}_D = \tilde{\mathbf{t}}_t \text{sur}(\partial B_t) = \pi \mu^f r_{\min} \mathbf{k} \cdot [\mathbf{u} - \mathbf{v}_c]. \quad (14)$$

Here, the dynamic viscosity is μ^f , the semi-minor axis is r_{\min} and the translational resistance tensor is \mathbf{k} , with its coefficients detailed in our previous work, [33]. Furthermore, the fluid velocity at the barycenter of the ellipsoid and its barycentric velocity are denoted as \mathbf{u} and \mathbf{v}_c , respectively.

3.3. Resultant force dyad

In the case of spatially uniform mass-specific bulk force density \mathbf{a} , the resultant force dyad $\mathbf{m} = \mathbf{M} \cdot \mathbf{F}^t$ can be expanded as

$$\mathbf{m} = \int_{\partial B_t} \tilde{\mathbf{t}}_t \otimes \xi \, da = \int_{\partial B_t} [\tilde{\boldsymbol{\sigma}} \cdot \mathbf{n}] \otimes \xi \, da = \int_{\partial B_t} [\xi \otimes \tilde{\boldsymbol{\sigma}} \cdot d\mathbf{a}]^t = \int_{B_t} [\text{div}(\xi \otimes \tilde{\boldsymbol{\sigma}})]^t \, dv = \tilde{\boldsymbol{\sigma}} \text{vol}(B_t), \quad (15)$$

where $da := \mathbf{n} \, da$ denotes the vectorial area element on ∂B_t . The resultant force dyad \mathbf{m} can be further parametrized in terms of $\text{vol}(B_0)$ by introducing the Kirchhoff-type stress $\tilde{\boldsymbol{\tau}} := \mathbf{J} \tilde{\boldsymbol{\sigma}}$ as $\mathbf{m} = \tilde{\boldsymbol{\tau}} \text{vol}(B_0)$. Finally, we can express the resultant force dyad $\mathbf{M} = \mathbf{m} \cdot \mathbf{F}^{-t}$ as

$$\mathbf{M} = \tilde{\mathbf{P}} \text{vol}(B_0) \text{ with } \tilde{\mathbf{P}} := \tilde{\boldsymbol{\tau}} \cdot \mathbf{F}^{-t}. \quad (16)$$

Note that by using (Jeffery and) Roscoe expressions for the traction (fluctuation) $\tilde{\mathbf{t}}_t$ exerted on an ellipsoidal body immersed in Stokes flow, expressions for $\tilde{\boldsymbol{\sigma}}$ and consequently $\tilde{\boldsymbol{\tau}}$ and $\tilde{\mathbf{P}}$ can be derived as detailed in our previous work, [33].

4. Time stepping for barycentric and shape dynamics

For soft ellipsoidal particles suspended in Stokes flow, the barycentric and shape dynamics equations are consistent with our previous work, [33], and read as

$$\dot{\mathbf{x}}_c = \mathbf{v}_c, \quad \dot{\mathbf{v}}_c = \mathbf{a}_G + \mathbf{a}_D = \underbrace{\frac{\rho_i^s - \rho^f}{\rho_i^s}}_{\beta_t} \mathbf{g} + \underbrace{\left[\frac{1}{m} \sqrt{f} \rho^f \pi r_{\min} \right]}_{1/\tau_D} \mathbf{k} \cdot [\mathbf{u} - \mathbf{v}_c], \quad (17)$$

and

$$\dot{\mathbf{F}} = \mathbf{A}, \quad \dot{\mathbf{A}} = \text{vol}(B_0) [\tilde{\mathbf{P}} - \mathbf{P}] \cdot \boldsymbol{\Theta}^{-1}, \quad (18)$$

respectively. Note that here β_t and τ_D denote the buoyancy-induced gravity reduction and the characteristic drag time, respectively. In the following, we detail the time stepping algorithm for the integration of the barycentric and shape dynamics equations of motion in discrete time steps $\Delta t := t^{n+1} - t^n$, with t^{n+1} and t^n discrete time points, over N discrete time steps Δt , i.e. over a finite time interval $T := \cup_{n=0}^{N-1} [t^{n+1} - t^n]$. At the discrete time point t^n we assume the barycenter position \mathbf{x}_c^n , the barycenter velocity \mathbf{v}_c^n , the deformation gradient \mathbf{F}^n as well as the material velocity gradient \mathbf{A}^n of the pseudo-rigid body to be given. Note that to describe the external loading for the time step Δt , we assume the fluid velocity \mathbf{u}^{n+1} together with the spatial fluid velocity gradient $\mathbf{f}_f^{n+1} := \mathbf{d}_f^{n+1} + \boldsymbol{\omega}_f^{n+1}$ at the discrete time point t^{n+1} to be given.

The barycenter dynamics for initially ellipsoidal particles are obtained similarly as presented in our previous work, see [33]. The barycenter position \mathbf{x}_c and the barycenter velocity \mathbf{v}_c are obtained using an implicit Euler backwards time integrator over Δt as

$$\mathbf{x}_c^{n+1} = \mathbf{x}_c^n + \Delta t \mathbf{v}_c^{n+1} \quad \text{and} \quad \mathbf{v}_c^{n+1} = \mathbf{v}_c^n + \Delta t \left[\beta_t^{n+1} \mathbf{g} + \frac{1}{\tau_D} \mathbf{k}^{n+1} \cdot [\mathbf{u}^{n+1} - \mathbf{v}_c^{n+1}] \right], \quad (19)$$

with

$$\beta_t^{n+1} := \beta_t(\bar{\mathbf{F}}^{n+1}) \quad \text{and} \quad \mathbf{k}^{n+1} := \mathbf{k}(\bar{\mathbf{F}}^{n+1}) \quad \text{with} \quad \bar{\mathbf{F}}^{n+1} = \mathbf{F}^{n+1} \cdot \mathbf{S}. \quad (20)$$

Note that \mathbf{F} describes the distortion, while $\bar{\mathbf{F}}^{n+1}$ additionally depends on \mathbf{S} , the shape and orientation tensor. Employing \mathbf{S} enables the modeling of pseudo-rigid bodies of initially ellipsoidal shape with arbitrary initial orientation. Observe that \mathbf{S} is constant throughout all time steps and only depends on the chosen shape and orientation of the initial ellipsoid.

The particle shape dynamics for initial ellipsoidal particles are obtained in the same fashion as presented in our previous work, see [33], using an implicit–explicit time integrator over Δt to update the elastic shape contribution \mathbf{F} as

$$\mathbf{F}^{n+1} = \mathbf{F}^n + \Delta t \mathbf{A}^{n+1} \quad \text{and} \quad \mathbf{A}^{n+1} = \mathbf{A}^n + \Delta t \text{vol}(B_0) [\tilde{\mathbf{P}}^* - \mathbf{P}^{n+1}] \cdot \boldsymbol{\Theta}^{-1}. \quad (21)$$

Observe the implicit update of the Piola stress \mathbf{P}^{n+1} and the implicit–explicit update (indicated by a superscript star) of the Piola-type stress $\tilde{\mathbf{P}}^*$ as

$$\mathbf{P}^{n+1} := \mathbf{P}(\mathbf{F}^{n+1}) \quad \text{and} \quad \tilde{\mathbf{P}}^* := J^{n+1} \tilde{\sigma}^*(\mathbf{F}^n, \mathbf{A}^n, \mathbf{S}; \mathbf{I}_f^{n+1}) \cdot [\mathbf{F}^{n+1}]^{-t}, \quad (22)$$

Note that the implicit–explicit update of the Cauchy-type stress $\tilde{\sigma}^*$ is modified for initially ellipsoidal particles compared to initially spherical particles as it depends additionally on the constant shape and orientation tensor \mathbf{S} to account for the initially ellipsoidal particle shape. Observe the dependence of $\tilde{\sigma}^*$ on $\bar{\mathbf{F}}^n = \mathbf{F}^n \cdot \mathbf{S}$ via \mathbf{n}_a^n and λ_a^n to update the ellipsoid shape and orientation, i.e. the particle frame of reference (pFoR) with the rotation matrix $\underline{\mathbf{Q}}^n := [\underline{\mathbf{Q}}_{aB}^n] = [\mathbf{n}_a^n \cdot \mathbf{E}_B]$, $a, B = 1, 2, 3$ and the ellipsoid's half axes $r_a^n = \lambda_a^n R$, $a = 1, 2, 3$, where $R = 1$ denotes the radius of the reference unit sphere. Identical to our previous work, [33], $\tilde{\sigma}^*$ depends on the contribution \mathbf{F}^n and \mathbf{A}^n via the spatial solid velocity gradient $\mathbf{l}_s^n = \mathbf{A}^n \cdot [\mathbf{F}^n]^{-1}$ with coefficients l_{sab}^n in the pFoR defined as $l_{sab}^n := \mathbf{n}_a^n \cdot \mathbf{l}_s^n \cdot \mathbf{n}_b^n$ as well as the fluid velocity gradient \mathbf{l}_f^{n+1} representing the external loading for Δt . Note that \mathbf{l}_f^{n+1} has the coefficients l_{fab}^* in the pFoR defined as $l_{fab}^* := \mathbf{n}_a^n \cdot \mathbf{l}_f^{n+1} \cdot \mathbf{n}_b^n$

5. Algorithm: Implicit-explicit time integrator

The step-by-step algorithm for the implicit–explicit time integrator for the shape dynamics of a pseudo-rigid body of initially ellipsoidal shape in the material configuration based on the deformation gradient is similar to the algorithm presented for initially spherical shape in our previous work, see [33]. Differences occur as we need to not only account for the distortion \mathbf{F}^n but rather for the total distortion $\bar{\mathbf{F}}^n = \mathbf{F}^n \cdot \mathbf{S}$. The modified algorithm is provided in the following.

Initialize First Increment :

- Set $\mathbf{x}_c^0 = \mathbf{0}$, $\mathbf{v}_c^0 = \mathbf{0}$ and $\mathbf{F}^0 = \mathbf{1}$, $\mathbf{A}^0 = \mathbf{0}$
- Set ellipsoidal shape and orientation: \mathbf{n}_a^0 , $\underline{\mathbf{Q}}_{aB}^0$, $\mathbf{S} := \sum_a R_a \mathbf{E}_a' \otimes \bar{\mathbf{E}}_a$ and r_a^0 , $a, A, B = 1, 2, 3$
- Compute Euler tensor $\boldsymbol{\Theta} = \frac{m}{5} \mathbf{S} \cdot \mathbf{S}^T$ in the material configuration
- Compute $\text{vol}(\mathcal{B}_0) = \det \mathbf{S} \text{vol}(\bar{\mathcal{B}}_0)$ with $\text{vol}(\bar{\mathcal{B}}_0) = \frac{4}{3} \pi R^3$ and $R = 1$

Increment Loop $n = 0, \dots, N - 1$

Pre-Process Increment:

- Read given fluid velocity and its spatial gradient from flow simulator \mathbf{u}^{n+1} and \mathbf{l}_f^{n+1}
- Compute coefficients in pFoR $l_{fab}^* = \mathbf{n}_a^n \cdot \mathbf{l}_f^{n+1} \cdot \mathbf{n}_b^n$, $a, b = 1, 2, 3$
- Compute spatial solid velocity gradient $\mathbf{l}_s^n = \mathbf{A}^n \cdot [\mathbf{F}^n]^{-1}$
- Compute coefficients in pFoR $l_{sab}^n = \mathbf{n}_a^n \cdot \mathbf{l}_s^n \cdot \mathbf{n}_b^n$, $a, b = 1, 2, 3$
- Compute Cauchy-type stress $\tilde{\sigma}^* = \tilde{\sigma}(r_a^n, l_{sab}^n, \underline{\mathbf{Q}}_{aB}^n; l_{fab}^*)$ with $\tilde{\sigma}_{AB}^* = \tilde{\sigma}_{mn}^* \underline{\mathbf{Q}}_{mA}^n \underline{\mathbf{Q}}_{nB}^n$, $a, A, B, m, n = 1, 2, 3$

Process Increment:

- Update distortion $\mathbf{F}^{n+1} = \arg \left\{ \mathbf{F}^{n+1} - \mathbf{F}^n - \Delta t \mathbf{A}^n - \Delta t^2 \text{vol}(\mathcal{B}_0) [\tilde{\mathbf{P}}^*(\mathbf{F}^{n+1}; \tilde{\sigma}^*) - \mathbf{P}(\mathbf{F}^{n+1})] \cdot \boldsymbol{\Theta}^{-1} \doteq \mathbf{0} \right\}$
- Update total distortion $\bar{\mathbf{F}}^{n+1} = \mathbf{F}^{n+1} \cdot \mathbf{S}$
- Update mass-specific reduced gravity force using the total distortion: $\mathbf{a}_G^{n+1} = \beta_g(\bar{\mathbf{F}}^{n+1}) \mathbf{g}$
- Update Eulerian principal directions using $\bar{\mathbf{F}}^{n+1}$: $\mathbf{n}_a^{n+1} = \text{eigenvec} \left\{ \bar{\mathbf{F}}^{n+1} \cdot [\bar{\mathbf{F}}^{n+1}]^t \right\}$, $a = 1, 2, 3$
- Update rotation matrix from iFoR to pFoR $\underline{\mathbf{Q}}_{aB}^{n+1} = \mathbf{n}_a^{n+1} \cdot \mathbf{E}_B$, $a, B = 1, 2, 3$
- Update principal values using $\bar{\mathbf{F}}^{n+1}$: $\lambda_a^{n+1} = \text{eigenval} \left\{ \bar{\mathbf{F}}^{n+1} \cdot [\bar{\mathbf{F}}^{n+1}]^t \right\}$, $a = 1, 2, 3$
- Update half axes $r_a^{n+1} = \lambda_a^{n+1}$, $a = 1, 2, 3$
- Update drag resistance tensor $\mathbf{k}^{n+1} = k(r_a^{n+1}, \underline{\mathbf{Q}}_{aB}^{n+1})$ with $k_{AB}^{n+1} = k_{mn}^{n+1} \underline{\mathbf{Q}}_{mA}^{n+1} \underline{\mathbf{Q}}_{nB}^{n+1}$, $a, A, B, m, n = 1, 2, 3$
- Update barycenter position $\mathbf{x}_c^{n+1} = [\mathbf{I} + \Delta t / \tau_D \mathbf{k}^{n+1}]^{-1} \cdot \left[\mathbf{x}_c^n + \Delta t \mathbf{v}_c^n + \Delta t^2 \mathbf{a}_G^{n+1} + \Delta t / \tau_D \mathbf{k}^{n+1} \cdot [\Delta t \mathbf{u}^{n+1} + \mathbf{x}_c^n] \right]$

Post-Process Increment:

- Update $\mathbf{v}_c^{n+1} = [\mathbf{x}_c^{n+1} - \mathbf{x}_c^n] / \Delta t$
- Update $\mathbf{A}^{n+1} = [\mathbf{F}^{n+1} - \mathbf{F}^n] / \Delta t$

Initialize Next Increment :

- Set $\mathbf{x}_c^n \leftarrow \mathbf{x}_c^{n+1}$, $\mathbf{v}_c^n \leftarrow \mathbf{v}_c^{n+1}$ and $\mathbf{F}^n \leftarrow \mathbf{F}^{n+1}$, $\mathbf{A}^n \leftarrow \mathbf{A}^{n+1}$ and $\mathbf{n}_a^n \leftarrow \mathbf{n}_a^{n+1}$, $\underline{\mathbf{Q}}_{aB}^n \leftarrow \underline{\mathbf{Q}}_{aB}^{n+1}$, $r_a^n \leftarrow r_a^{n+1}$, $a, B = 1, 2, 3$

End Increment Loop

Note that the employed Newton Raphson scheme to update the distortion \mathbf{F}^{n+1} converges quadratically and typically in 3 iterations to take the residual below $1e-12$.

6. Demonstrative examples

In the following, we will first validate our extended model using experimental and numerical studies from the literature for quasi-rigid and soft ellipsoidal particles. This is followed by a comparison of the effects of deformability for some well-known fluid flow cases, such as a laminar pipe flow ($Re = 137$ and $Stk = 0.01$), a lid-driven cavity flow ($Re = 470$ and $Stk = 0.0023$) and a simplified bifurcation ($Re = 500$ and $Stk = 0.5 \times 10^{-2} - 0.5$). Throughout the demonstrative examples (unless explicitly stated otherwise), the characteristic scales for non-dimensionalization are the length scale d_{eq} (initial volume-equivalent particle diameter), the time scale $\dot{\gamma}^{-1}$ (inverse fluid shear rate) and the fluid pressure/stress scale $\mu^f \dot{\gamma}$. Here, μ^f denotes the dynamic viscosity of the fluid. In the following, we use the capillary number Ca to quantify the softness of the particle, which represents the ratio of the viscous forces in the fluid to the elastic forces in the particle, [30] as

$$Ca = \frac{\mu^f \dot{\gamma}}{\mu^s}. \quad (23)$$

with μ^s denoting the particle shear modulus. Note that a larger Ca value is associated with a softer particle, [30]. Furthermore, we can define the particle shear Reynolds number using the fluid shear rate $\dot{\gamma}$ as

$$Re_{\dot{\gamma}} = \frac{\dot{\gamma} d_{eq}^2}{\nu^f}. \quad (24)$$

Note that a key assumption of the Jeffery-Roscoe solution is creeping flow with $Re_{\dot{\gamma}} \ll 1$ locally.

In addition, Stk denotes the Stokes number, which describes the ratio of the characteristic particle response time τ^p to a characteristic time of the flow τ^f . The Stokes number of a particle with volume equivalent sphere diameter d_{eq} is defined as

$$Stk = \frac{\tau^p}{\tau^f} = \frac{\rho^p}{\rho^f} \frac{d_{eq}^2 U}{18 \nu^f L}. \quad (25)$$

The characteristic time scales of the particle τ^p and the flow τ^f are defined as follows:

$$\tau^p = \frac{\rho^p}{\rho^f} \frac{d_{eq}^2}{18 \nu^f}, \quad \tau^f = \frac{L}{U}, \quad (26)$$

where L and U denote a characteristic length and velocity of the flow problem, respectively. Note that we neglect the pressure gradient and added mass force as we assume that $\rho^p \gg \rho^f$ and/or $Stk \ll 1$.

6.1. Shape dynamics of soft ellipsoidal particles in simple shear flow

In this section, we study the dynamics of neutrally buoyant deformable ellipsoidal particles suspended in a simple shear flow. As observed in our previous work [33], and by other authors, [29,30], initially spherical particles, when suspended in simple shear flow, can reach a steady state in shape and orientation. This is not the case for soft particles with an initially ellipsoidal shape. It is known, [21,31] that ellipsoidal particles, when suspended in simple shear flow, exhibit either trembling (TR) or tumbling (TU) dynamics. Tumbling dynamics occur when the elastic forces in the particle, which tend to preserve the initial ellipsoidal particle shape, are sufficiently strong compared to the hydrodynamic forces, i.e. the major axis of the deformed particle appears to oscillate between two angles. On the other hand, trembling dynamics occurs when the hydrodynamic forces become sufficiently strong compared to the elastic forces, i.e. the major axis of the particle appears to perform a complete (however unsteady) rotation. Note that all material lines are in constant rotation, thus the TU and TR regime can visually only be distinguished by the apparent motion of the long axis of the particle. In general, TU and TR can be distinguished by observing the lengths of two material lines l_a and l_c , which initially coincide with the semi-axes in the shear plane, i.e. r_1 and r_3 , where we use the definition $r_1 \geq r_2 \geq r_3$. Due to the constant deformation of the material inside the deforming particle, both lines continue to rotate in the same direction according to the solid spin tensor \mathbf{w}_s . If a particle exhibits tumbling dynamics, the length of l_a will always be larger than l_c . In this case, the particle major axis in the shear plane appears to perform full rotations. However, if at any time $l_c > l_a$, the observed major axis does not perform a full rotation and appears to oscillate between two orientations. This dynamic behavior is referred to as trembling. Using these two dynamic behaviors, a phase diagram can be constructed in which the phase boundary is consequently defined when at any point in time $l_c = l_a$.

6.1.1. Dynamics of oblate ellipsoids suspended in simple shear flow

First, we investigate the shape dynamics of oblate ellipsoids ($\lambda_1 = \lambda_2$) suspended in simple shear flow. As a reference, we use the results of Sanagavarapu et al. [21]. We validate our model by reproducing the study of [21] for oblate particles suspended in simple shear flow. In this context, we set the initial particle orientation such that the particle plane $E'_1 - E'_3$ lies in the shear plane $E_1 - E_2$ and $E'_3 = E_2$ and consequently $E'_1 = -E_1$. This corresponds to the setup used in [21]. For the sake of clarity, the setup is visualized in Fig. 3.

Observe that the initial particle major semi-axis r_1 and minor-semi axis r_3 lie in the shear plane. In the scope of our work, we use $r_1 \geq r_2 \geq r_3$ and thus the aspect ratio as $\lambda_1 = r_1/r_3$ and $\lambda_2 = r_2/r_3$ with $\lambda_1 \geq \lambda_2$. In the work of [21], however, the in-shear plane aspect ratio ω_1 and the out-of-shear plane aspect ratio ω_2 are given to describe the shape dynamics. Note that for the initially oblate particle chosen with the initial particle plane $E'_1 - E'_3$ in the shear plane $E_1 - E_2$, $\omega_1(t=0)$ initially coincides with $\lambda_1(t=0)$.

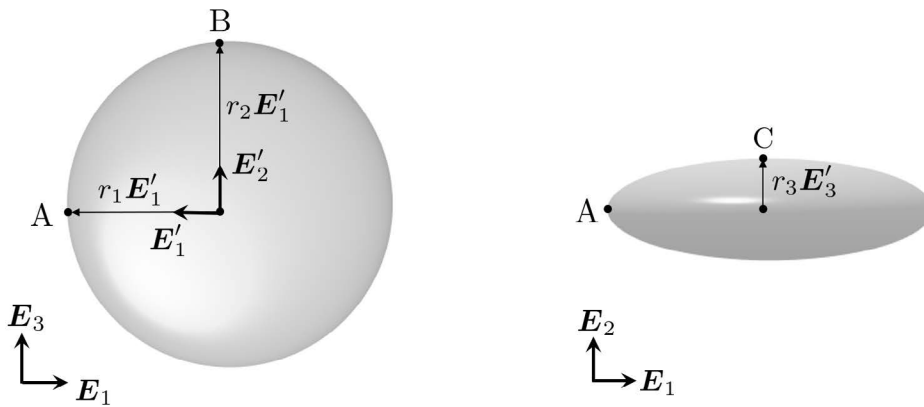


Fig. 3. Schematic visualization of the semi-axis lengths and orientations of the principal axes of the employed initially oblate particle. The particle frame of reference is labeled E'_i and the global frame of reference is labeled E_i with $i = 1, 2, 3$. The particle semi-axis lengths are denoted as r_i , $i = 1, 2, 3$. Note that we employ $r_1 \geq r_2 \geq r_3$. The material points A, B, C are initially located on the semi-axis.

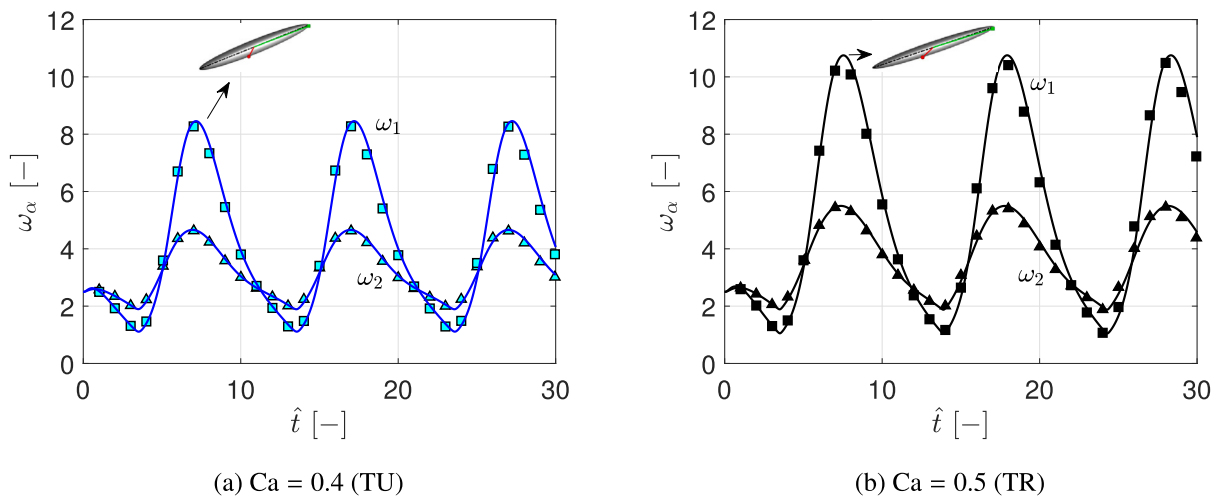


Fig. 4. Dynamics of an initially oblate ellipsoid exhibiting trembling and tumbling dynamics with an initial in-shear plane aspect ratio of $\omega_1(t=0) = 2.5$ (initial out-of-shear plane aspect ratio $\omega_2(t=0) = 2.5$). Note that the types of dynamics exhibited are denoted either by TR for trembling or TU for tumbling. Present model results: ■ $Ca = 0.4$, ■ $Ca = 0.5$. Reference results are presented using symbols in the respective color of the present model. In (a) we insert a picture of the particle shape at $\hat{t} \approx 7$, while in (b) we display the particle shape at $\hat{t} \approx 7.5$. These particle shapes coincide with the maximum ω_α for the respective particle softness. (For interpretation of the references to color in this figure legend, the reader is referred to the web version of this article.)

The examined oblate particles have an initial in-shear/out-of-shear plane aspect ratio of $\omega_1(t=0) = \omega_2(t=0) = 2.5$. The softness parameter of the particles is selected as $Ca = 0.4$ or $Ca = 0.5$, whereby the first leads to TU dynamics, while the second results in TR dynamics, [21]. Fig. 4(a,b) illustrates the dynamic behavior of the in-shear/out-of-shear plane aspect ratios ω_α , $\alpha = 1, 2$ for $Ca = 0.4$ and $Ca = 0.5$, respectively. As shown in Fig. 4(a), we achieve perfect agreement in the transient deformation for the initially oblate particle in the TU regime compared to the results of [21]. Fig. 4(b) shows that the novel method is also able to reproduce the transient deformation behavior for initially oblate particles in the TR regime.

In the following, we present snapshots of the deformation of the particles in the shear plane over a time span of $t = 20$ for the oblate particles under consideration. The black line represents the long axes of the particle. In addition, we highlight two material lines l_a and l_c , which initially coincide with the particle semi-axis in the shear plane. Note that we choose the color scheme so that the smaller material line is displayed in red, i.e. $\min(l_a, l_c)$, while the longer line is colored in green, i.e. $\max(l_a, l_c)$.

As highlighted, the deformation of the particles depends strongly on the softness of the particles. For particles with $Ca = 0.4$, the elongation of the particles is less than for particles with $Ca = 0.5$. Furthermore, we observe that the orientation of the particles is also slightly modified. However, we find that the orientations of the material lines are approximately identical, see the red ($\min(l_a, l_c)$) and green ($\max(l_a, l_c)$) line displayed in Fig. 5.

Next, we visualize the deformation of the particles to illustrate the difference between the tumbling and trembling regimes, see Fig. 6. Recalling the definition of the red and green material line, we find that for $Ca = 0.5$ at $23.5 < \hat{t} < 24$, the lines' coloring is

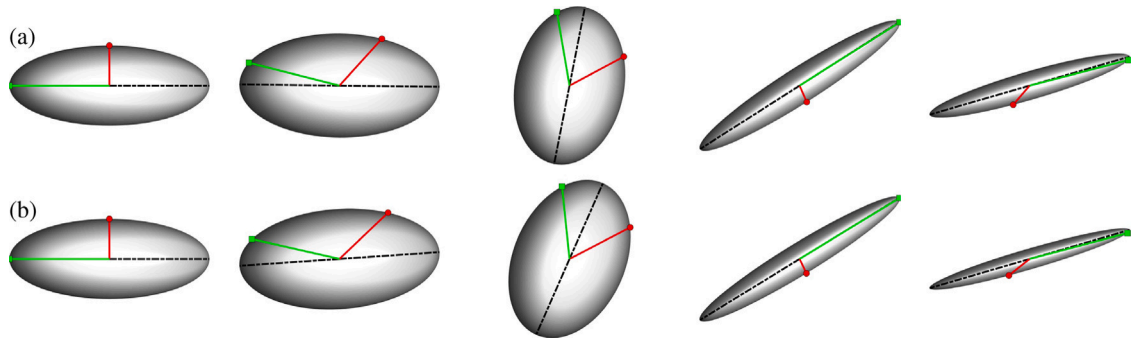


Fig. 5. Snapshots of initially oblate ellipsoid of either (a) $Ca = 0.4$ (TU) or (b) $Ca = 0.5$ (TR) suspended in simple shear flow. The displayed time step are from left to right $\hat{t} = [0, 2, 4, 6, 8]$. Note that the types of dynamics exhibited are denoted either by TR for trembling or TU for tumbling. Here \blacksquare highlights the particle's major axis in the shear plane. The lines l_a and l_c pointing to the material point A and C, respectively, are highlighted with the following colors: \blacksquare $\max(l_a, l_c)$, \blacksquare $\min(l_a, l_c)$. (For interpretation of the references to color in this figure legend, the reader is referred to the web version of this article.)

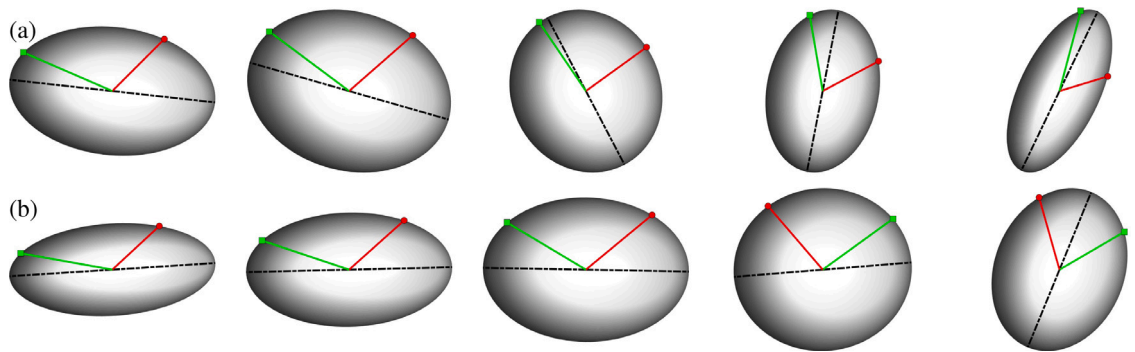


Fig. 6. Snapshots of initially oblate ellipsoid of either (a) $Ca = 0.4$ (TU) or (b) $Ca = 0.5$ (TR) suspended in simple shear flow. The displayed time step are from left to right $\hat{t} = [22.5, 23, 23.5, 24, 24.5]$. Note that the types of dynamics exhibited are denoted by either TR for trembling or TU for tumbling. Here \blacksquare highlights the particle major axis in the shear plane. The lines l_a and l_c pointing to the material point A and C, respectively, are presented with the following colors: \blacksquare $\max(l_a, l_c)$, \blacksquare $\min(l_a, l_c)$. (For interpretation of the references to color in this figure legend, the reader is referred to the web version of this article.)

reversed indicating that at some intermediate instance the length of the green and the red line are identical and thus trembling is observed.

Recall that in the TU regime, the length of l_a will always be larger than l_c , thus the particle semi-major axis r_1 conducts full rotations. However, if at any instance $l_c > l_a$, the major axis in the shear plane (black line) does not perform a complete rotation and appears to oscillate between two orientations, which is defined as TR dynamics.

6.1.2. Tumbling and trembling phase diagram for initially oblate/prolate particles suspended in simple shear flow

Since the switch between trembling and tumbling dynamics depends on the initial particle shape, i.e. the initial in-shear/out-of-shear plane aspect ratio, as well as the particle softness Ca , it is useful to represent the different dynamic regimes in a phase diagram. Fig. 7 shows the phase diagram for initially prolate and oblate particles. Note that for comparison with the results of Sanagavarapu, [21] for initially prolate (and triaxial) particles, the two largest initial particle long axes r_1 and r_2 are located in the shear plane, while the particle minor axis r_3 ($r_2 = r_3$ for prolate particles) is located outside the shear plane. Note that Sanagavarapu, [21], defines the in-shear plane aspect ratio ω_1 for prolate (and triaxial) particles as the ratio of the smaller semi-axis to the longer semi-axis in the shear plane. The out-of-shear plane aspect ratio ω_2 is defined as the ratio of the semi-axis outside the shear plane to the longer half-axis in the shear plane. This leads to $\omega_1(t=0) \leq 1$ and $\omega_2(t=0) = 1$ for initially prolate ellipsoids.

As highlighted, we achieve an excellent agreement between the reference results, see [21], and the results obtained with our novel soft particles model for ellipsoidal particles.

6.1.3. Initially triaxial particles suspended in simple shear flow

Finally, we suspend initially triaxial ($r_1 \neq r_2 \neq r_3$) ellipsoids in simple shear flow. As shown by Sanagavarapu et al. [21], the TU-TR phase boundary for soft triaxial ellipsoids is a two-dimensional surface since it depends on Ca , $\omega_1(t=0)$ and $\omega_2(t=0)$. As a reference, we employ the results reported by Sanagavarapu et al. [21]. Note that the authors provided the upper and lower bounds for the TU-TR phase boundary for different cross-sections of the phase diagram. Since their framework requires surface discretization and is therefore computationally much more intensive, Sanagavarapu et al. [21] chose larger discrete steps of $\Delta Ca = 0.05$. Thus, their

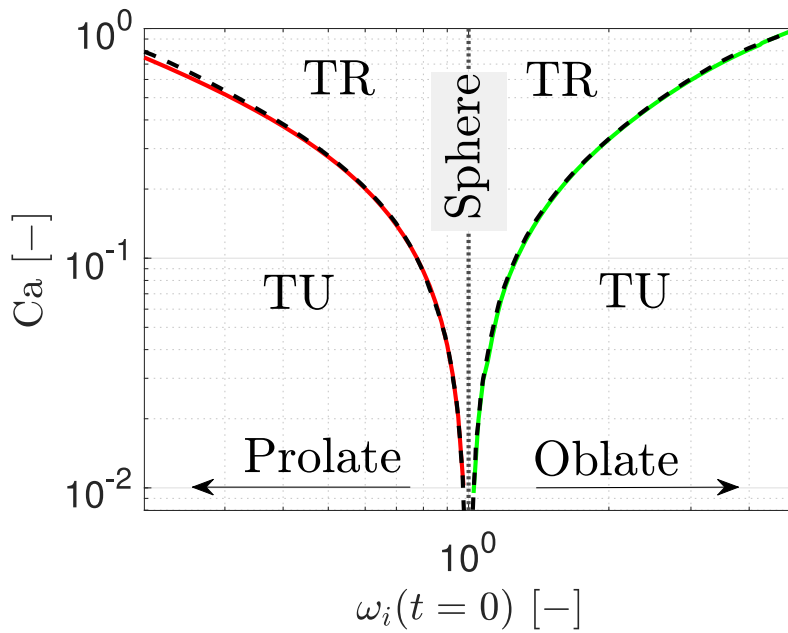


Fig. 7. Tumbling-trembling phase diagram of initially oblate and prolate ellipsoids suspended in simple shear flow. Note that the types of dynamics exhibited are denoted by TR for trembling or TU for tumbling. ■ Sanagavarapu et al. [21], ■ present model. (For interpretation of the references to color in this figure legend, the reader is referred to the web version of this article.)

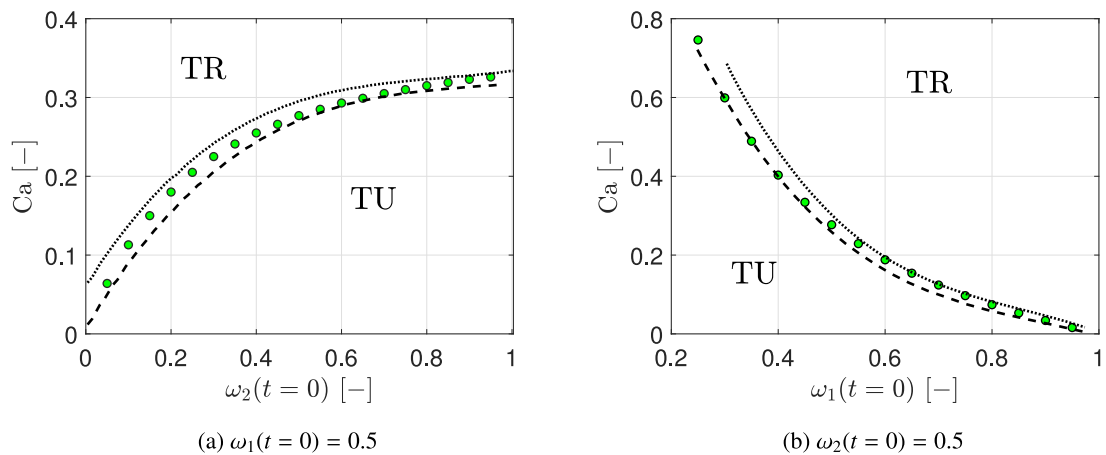


Fig. 8. Sections of the tumbling-trembling phase diagram of an initially triaxial ellipsoid in simple shear flow for either fixed (a) $\omega_1(t = 0) = 0.5$ or (b) $\omega_2(t = 0) = 0.5$. The trembling and tumbling regime are labeled TR and TU, respectively. ■ Sanagavarapu et al. [21], ● present model.

reported results can deviate from the true phase boundary by one step size ($\Delta Ca = 0.05$). Since our novel model is computationally highly efficient, we can choose a much smaller discretization step for Ca, i.e. $\Delta Ca = 0.005$. Consequently, our results can deviate from the true phase boundary at most by $\Delta Ca = 0.005$, i.e. we here achieve a ten times higher accuracy.

Fig. 8(a) presents the TU-TR phase diagram for soft initially ellipsoidal particles for the $\omega_1(t = 0) = 0.5$ cross-section. As can be seen, the obtained phase boundary lies between the reported upper and lower bounds (Sanagavarapu et al. [21]). Fig. 8(b) displays the $\omega_1(t = 0) = 0.5$ cross-section of the TU-TR phase diagram. Again, it can be seen that our novel model can accurately capture the phase boundary between tumbling and trembling, as the results are enclosed by the upper and lower bounds reported by Sanagavarapu et al. [21]. Recall that the results were resolved with 10 times smaller ΔCa steps than given in the references, as the present method requires significantly less computational effort. Therefore, the maximum deviation from the true phase diagram is reduced by a factor of 10 compared to the reference results.

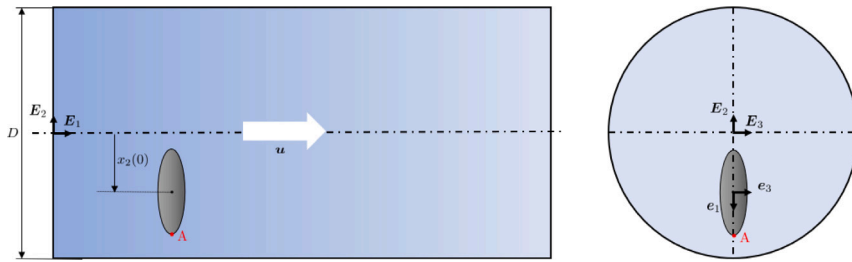


Fig. 9. Sketch of the circular tube and initial position of the particle in the cross-section. Observe that A is defined as the material point on the particle surface that is initially located at $r_1 e_1$. Note that the particle size is strongly enlarged for visualization purposes as $d_{eq} \ll D$.

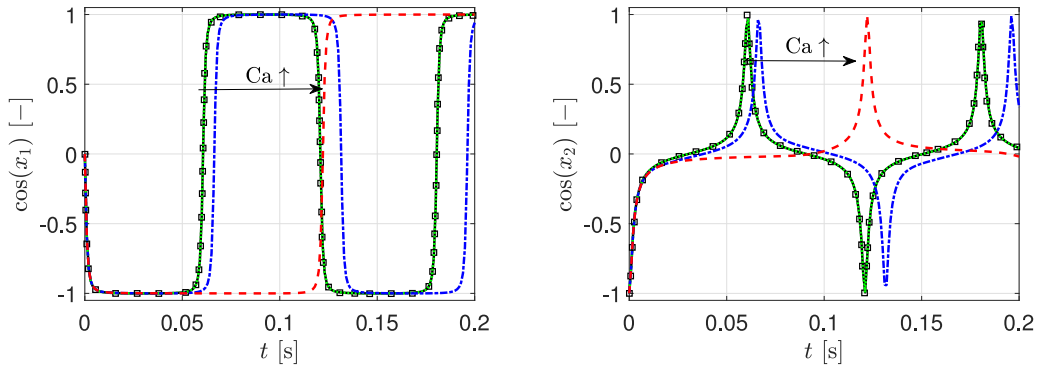


Fig. 10. Direction cosines of a vector pointing from the barycenter to a material point A (see Fig. 9) located initially at the end of the semi-major axis of the prolate ellipsoidal particle for $\lambda_1 = 14$ for particles with different softness: \square Cui et al. ($U_{max} = 0.97$ m/s) [38], present model: \blacksquare $Ca \rightarrow 0$, \blacksquare $Ca = 0.01$, \blacksquare $Ca = 0.05$, \blacksquare $Ca = 0.1$. (For interpretation of the references to color in this figure legend, the reader is referred to the web version of this article.)

6.2. Soft particles suspended in laminar pipe flow

In this section, we use our novel approach to study soft ellipsoidal particles suspended in laminar pipe flow. The experimental study by Tian et al. serves as a reference, [37]. Here, the authors investigated a rigid ellipsoidal particle suspended in a laminar (air) flow ($Re = 137$ with $\rho^f = 1.208$ kg/m³ and $\nu^f = 1.491 \times 10^{-5}$ mm²/s) in a circular channel with length $L = 0.7$ m and diameter $D = 4.2$ mm. Cui et al. [38], numerically replicated the results of Tian et al. [37], and suggested an average inflow velocity of $\bar{U} = 0.485$ m/s to match the experimental results. The rigid ellipsoidal particle used in the reference literature has a prolate shape with semi-minor axis $r_3 = 0.5$ μ m and aspect ratio $\lambda = 14$. Using the resulting volume equivalent diameter $d_{eq} = 2.41$ μ m and the fluid velocity at the initial particle location $u = 0.371$ m/s, while assuming an initially zero particle velocity, we estimate a worst-case particle Reynolds number $Re_p = d_{eq} u / \nu^f = 0.05$. However, this worst-case estimate never occurs within the simulation, as the particle velocity is initialized with the local flow velocity. Consequently, the assumption $Re_p \ll 1$, required by the Jeffery-Roscoe model, is satisfied.

The density of the particle is given as $\rho^p = 2560$ kg/m³ (i.e. $\rho^p \gg \rho^f$) and its response time is $\tau^p = 0.046$ ms with Stokes number of $Stk = 0.01$. The initial position of the particle is in the plane x_1 - x_2 with an initial position of $x_2 = -1.65$ mm. The initial position and orientation of the particle are shown in Fig. 9. At the injection position, we evaluated the flow vorticity as $\omega^f = 726,95$ s⁻¹.

Fig. 10(a,b) presents the obtained directional cosine values for quasi-rigid particles as well as soft particles obtained with our novel approach and the reference results of Cui et al. [38] for rigid particles. In the following, we present the direction cosine of the material line l_a connecting the particle center to the material point A, see Fig. 9. The selected material line coincides with the particle semi-major axis of the initially prolate ellipsoidal particle at the beginning of the simulation. Note that only for quasi-rigid particles does the selected material line always coincide with the semi-major axis during the entire simulation.

As shown in Fig. 10(a,b), we find an excellent agreement of the direction cosines of the quasi-rigid particle $Ca \rightarrow 0$ with the reference results. This confirms the ability of our novel soft particle approach to accurately capture the rotational motion of the investigated soft particles in the limit of a quasi-rigid body. By increasing the particle softness ($Ca \uparrow$), see Fig. 10(a,b), the deviations in the direction cosines of the material line l_a vary increasingly compared to the quasi-rigid particle reference. We find that the softer the particle under consideration, the longer the orbital period of the investigated material line.

6.2.1. Influence of deformability on particle trajectory in laminar pipe flow

Next, we inject soft particles into the laminar pipe flow. The setup of the pipe flow is identical to that described in the previous section. Here we use soft initially prolate particles ($\lambda_1 > \lambda_2$ and $\lambda_2 = 1$). The particles are tracked until they are deposited.

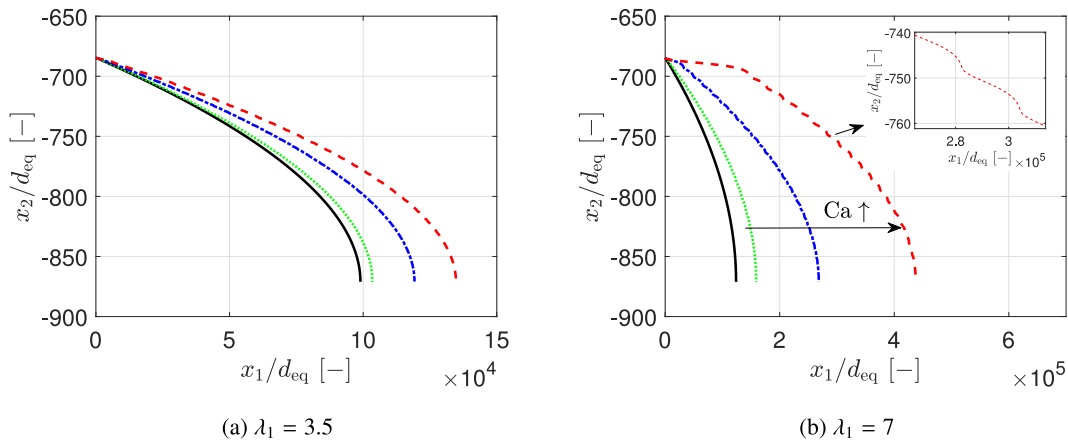


Fig. 11. Comparison of trajectory of initially prolate ellipsoids of different particle softness suspended in pipe flow: \blacksquare $Ca \rightarrow 0$, \blacksquare $Ca = 0.2$, \blacksquare $Ca = 0.5$, \blacksquare $Ca = 0.9$. (For interpretation of the references to color in this figure legend, the reader is referred to the web version of this article.)

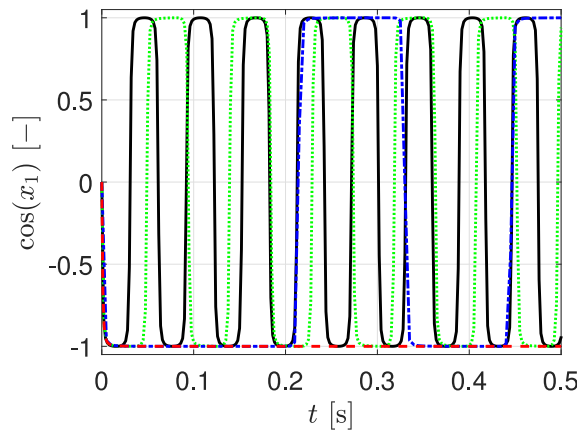


Fig. 12. Comparison of direction cosine of the material point A initially located on the particle semi major-axis to the x_1 direction for initially prolate ellipsoids of different particle softness suspended in pipe flow: \blacksquare $Ca \rightarrow 0$, \blacksquare $Ca = 0.2$, \blacksquare $Ca = 0.5$, \blacksquare $Ca = 0.9$. (For interpretation of the references to color in this figure legend, the reader is referred to the web version of this article.)

Fig. 11(a) displays the particle trajectory of soft particles with an initial aspect ratio $\lambda_1 = 3.5$ for particles of different softness, i.e. $Ca = [0, 0.2, 0.5, 0.9]$. As observed, particles with increased softness travel significantly faster in the streamwise direction. We attribute this to soft particles exhibiting both tumbling and trembling dynamics (interplay of elastic restoring forces and hydrodynamic forces), while rigid ellipsoidal particles only exhibit tumbling motion. For example, particles with a softness of $Ca = 0.25$ move about $4500 d_{eq}$ further in the streamwise direction than their quasi-rigid counterpart ($Ca \rightarrow 0$). For particles with $Ca = 0.9$, the deviations from the quasi-rigid reference increase to more than $35000 d_{eq}$ in the direction of flow. For soft particles with an initial aspect ratio $\lambda_1 = 7$ there is an identical trend, with softer particles moving further in the streamwise direction, see Fig. 11(b). Furthermore, we observe that an increase in the initial particle aspect ratio leads to an increase in the deviation between soft particles and their quasi-rigid reference in streamwise traveling direction. For example, particles with a softness of $Ca = 0.25$ and $Ca = 0.9$ travel more than $35000 d_{eq}$ and $313000 d_{eq}$ further in the flow direction than their quasi-rigid counterpart ($Ca \rightarrow 0$). Furthermore, we observe that increasing oscillations in the particle trajectory can be observed due to tumbling and trembling dynamics, especially for more elongated particles in combination with higher particle softness, see 11(c).

Fig. 12 presents the direction cosine of the material line l_a . Note that for rigid particles, this material line always coincides with the semi-major axis of the particle, which is not the case for soft particles. However, for elongated particles, the deviation between the position of l_a and the semi-major axis is small. As highlighted, we observe that an increasing softness of the particles leads to a longer orbit time of l_a and an increased alignment time with the streamwise direction. This indicates (since the position of l_a and the semi-major axis are comparable) a prolonged alignment time of the particle semi-major axis of the particle with the streamwise direction. As a result, we observe a reduced settling velocity, which in turn leads to an increased distance traveled in the streamwise direction before deposition.

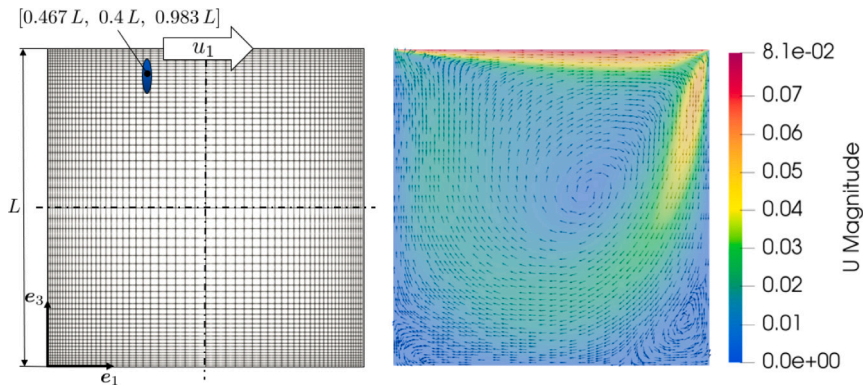


Fig. 13. Sketch of computational domain and particle injection position and the flow field ($Re = 470$) inside the lid-driven cavity in the $x_2/L = 0.4$ plane. The computational grid of $L = 0.1$ m for the fluid domain is discretized with a grid resolution of $60 \times 60 \times 60$. The particle is released close to the top wall with an initial position of $[0.467 L, 0.4 L, 0.983 L]$.

6.3. Soft particles in lid-driven cavity flow

Next, we study particles suspended in a lid-driven cavity flow, which is a common benchmark, [38]. The lid-driven cavity flow has been widely studied (experimentally: [39,40], analytically: [41], and numerically: [38,42]). Cui et al. [38], numerically replicated the experimental results of Tsorngr et al. [39], who studied the motion of rigid spheres ($d_p = 3$ mm and $\rho^p = 1210$ kg/m) suspended in a viscous 3D flow in a closed cubic cavity. Cui et al. [38], extended the study by numerically investigating the orientational and barycentric dynamics of suspended rigid prolate ellipsoidal particles in the cavity flow using an identical setup as Tsorngr et al. [39].

6.3.1. Quasi-rigid body limit

In the following, we employ an identical setup as in the numerical study by Cui et al. [38], who studied rigid ellipsoids in a lid-driven cavity flow. This allows us to validate our novel model in the rigid body limit ($Ca \rightarrow 0$). The dimensions and boundary conditions for the lid-driven cavity are consistent with the study by Cui et al. [38], and are replicated in Fig. 13 for convenience. Observe that the initial particle position and orientation of the injected particle are visualized. The lid of the cavity moves at a constant velocity $U = 0.0813$ m/s and is filled with a fluid (water–glycol mixture) with kinematic viscosity $\nu^f = 17.3$ mm²/s, resulting in a Reynolds number of $Re = 470$.

Note that at all walls we set the no-slip boundary condition. In agreement with Cui et al. [38], we consider both the drag force f_D and the reduced gravitational force f_G . In the following, we assume that suspended particles colliding with the upper wall leave the domain, while for all other walls, it is assumed that the particles stick.

In agreement with Cui et al. [38], we suspend two quasi-rigid prolate ellipsoids ($\lambda_2 = 1$) of volume equivalent diameter $d_{eq} = 3$ mm with an aspect ratio of either $\lambda_1 = 2.0$ or $\lambda_1 = 5.0$ in the lid-driven cavity flow.

The density ratio of fluid to particle is set to $\rho^* = [\rho^f - \rho^p]/\rho^f = +0.05\%$. The maximum tracking time is selected as $t_{max} = 5$ s ($\approx 172.4 \tau^p$). Fig. 14 presents the trajectory of a pseudo-rigid body in the rigid body limit together with the results of Cui et al. [38], who studied rigid prolate ellipsoids. As shown in Fig. 14, we achieve an excellent agreement of the particle trajectory with the pseudo-rigid body approach with $Ca \rightarrow 0$ compared to the reference results. This test case clearly demonstrates the applicability of the novel pseudo-rigid body approach with initially ellipsoidal shapes to replicate ellipsoidal particle motions in flows in the rigid body limit.

The worst-case particle Reynolds number for the above case can be estimated using $d_{eq} = 3$ mm and the fluid velocity at the initial particle location $u^0 = 0.367$ m/s. Consequently, the worst-case particle Reynolds number results as $Re_p = d_{eq}u/\nu^f \approx 64$. Recall that, this estimate is obtained with the assumption of an initially zero particle velocity and a constant fluid velocity of u^0 . However, this worst-case does not occur in the scope of this simulation, as the particle velocity is initialized with the local flow velocity and thus the relative velocity magnitude throughout the simulation is $u_{rel} \ll u$. Note that the average relative velocity observed throughout the simulation in the case of $\lambda = 5$ is $u_{rel} \approx 3.3 \times 10^{-4}$ m/s and, consequently, $Re_p \approx 0.057 \ll 1$.

6.3.2. Pseudo-rigid body cases

Next, we employ soft initially prolate ellipsoidal particles, i.e. $Ca > 0$, to analyze the influence of the particle softness on the particle trajectory. In this context, we investigate the influence of particle softness on initially prolate particles with equivalent diameter $d_{eq} = 3$ mm and particle density $\rho^p = 1209$ kg/m. The particle injection position is kept at $[0.467 L, 0.4 L, 0.983 L]$ and the initial particle aspect ratio is set to either $\lambda_1 = 1$ (sphere), $\lambda_1 = 2$, $\lambda_1 = 5$ or $\lambda_1 = 8$.

For initially spherical particles, see Fig. 15(a), we observe strong deviations between rigid particles and soft particles. While the rigid particle gets trapped in the lower right corner of the cavity, the soft particles continue to travel through the entire cavity.

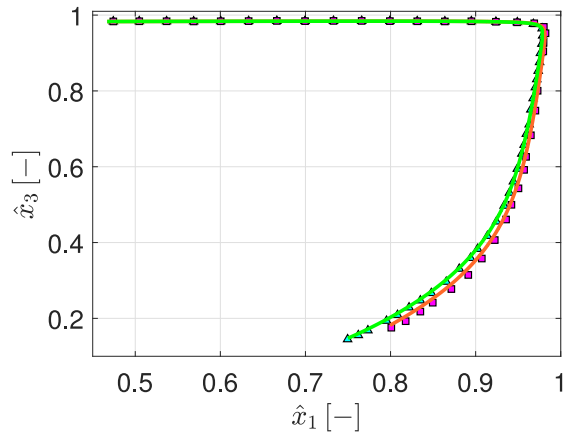


Fig. 14. Trajectory of (initially) prolate ellipsoidal particles in the $x_2/L = 0.4$ plane with $\rho^* = +0.05\%$. Present model for pseudo rigid bodies with $Ca \rightarrow 0$ (quasi-rigid): ● $\lambda = 5$, ■ $\lambda = 2$. Reference results by Cui et al. [38] for rigid ellipsoids ($\rho^* = +0.05\%$): ▲ $\lambda = 5$, ■ $\lambda = 2$. (For interpretation of the references to color in this figure legend, the reader is referred to the web version of this article.)

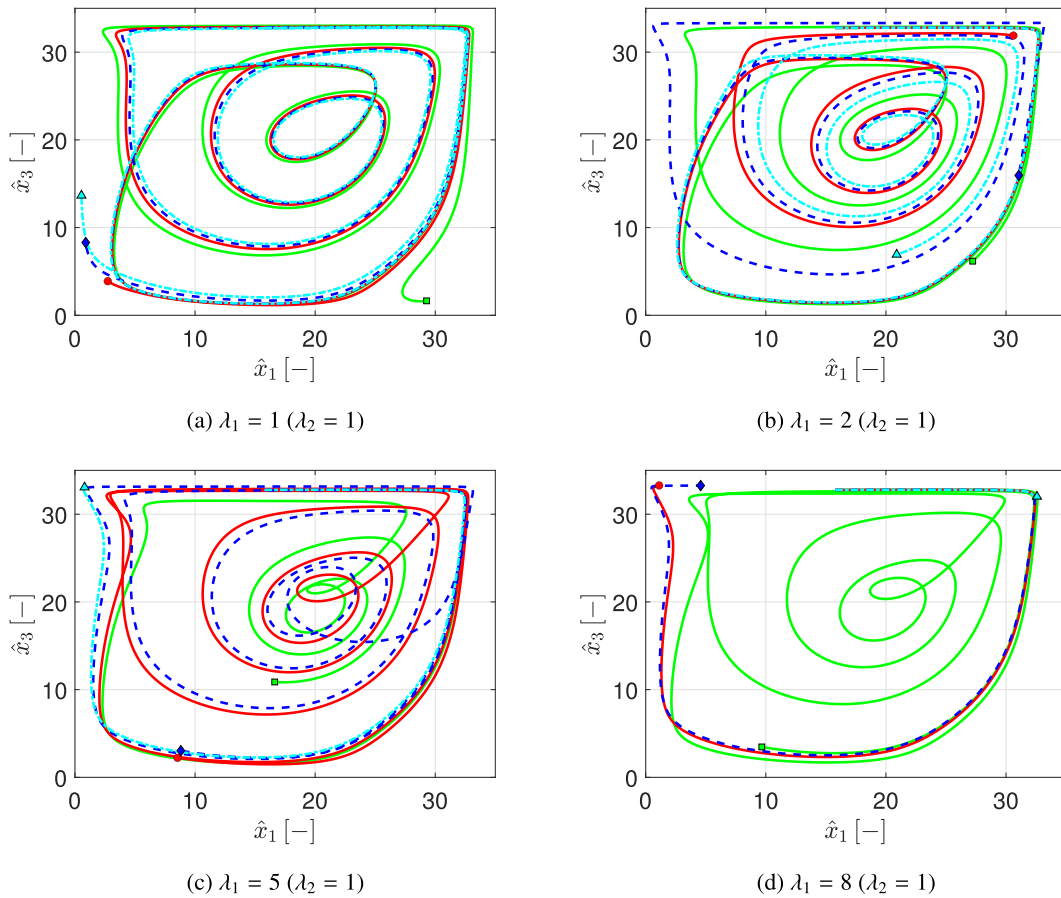


Fig. 15. Trajectory of soft initially prolate ($\lambda_2 = 1$) ellipsoidal particles ($\lambda_1 = 1$ (a), $\lambda_1 = 2$ (b), $\lambda_1 = 5$ (d), $\lambda_1 = 8$ (c)) of diameter $d_{eq} = 3$ mm and density $\rho^P = 1209.395$ kg/m³. The particle is released in the $x_2/L = 0.4$ plane at initial position $[0.467L, 0.4L, 0.983L]$. The maximum tracking time is set to 100 s. The Capillary number of the respective particles is computed depending on the shear rate at the injection position of the particle. Present model with Ca : ■ 0.001, ■ 0.25, ■ 0.5, ■ 0.75. The final position of the corresponding particle (position at $t = 100$ s) is highlighted with a symbol in the corresponding color. (For interpretation of the references to color in this figure legend, the reader is referred to the web version of this article.)

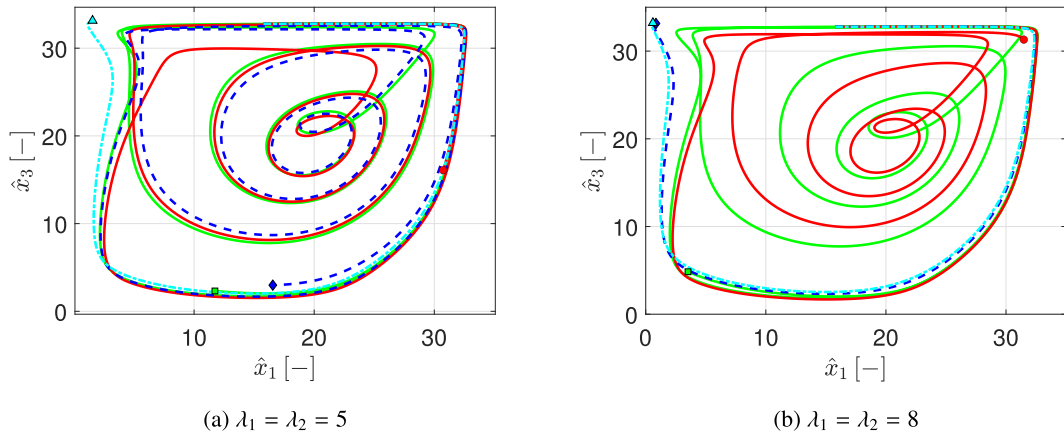


Fig. 16. Trajectory of soft initially oblate ellipsoidal particles ($\lambda_1 = \lambda_2 = 2$) of diameter $d_{eq} = 3$ mm and density $\rho^p = 1209.395$ kg/m³. The particle is released in the $x_2/L = 0.4$ plane at initial position $[0.467L, 0.4L, 0.983L]$. The maximum tracking time is set to 100 s. The Capillary number of the respective particles is computed depending on the shear rate at the injection position of the particle. Present model with Ca: ■ 0.001, ■ 0.25, ■ 0.5, ■ 0.75. The final position of the corresponding particle (position at $t = 100$ s) is highlighted with a symbol in the corresponding color chosen for the specific particle softness. (For interpretation of the references to color in this figure legend, the reader is referred to the web version of this article.)

It can also be observed that the deviations from the rigid particle reference increase with increasing softness of the particle. As shown in Fig. 15(b), the deviations between rigid and soft particles are increased for initially elongated prolate ellipsoids compared to initially spherical particles. This leads to significant deviations in the final particle position for all considered soft particles. For an even larger initial aspect ratio, i.e. $\lambda_1 = 5$, see Fig. 15(c), and $\lambda_1 = 8$, see Fig. 15(d), the deviations between the final positions become even more pronounced with increasing Ca. Furthermore, it can be observed that only particles with an initial aspect ratio $\lambda_1 = 5$ and a particle softness $Ca = 0.75$ leave the cavity via the upper wall. For particles with an initial aspect ratio $\lambda_1 = 8$ already slightly soft particle leave the cavity, i.e. $Ca \geq 0.25$, while the particle with $Ca \geq 0.75$ sticks to the right wall. We attribute the variation in particle trajectories for different Ca to the competition between elastic restoring forces and hydrodynamic forces. As this is a time-dependent phenomenon, even small differences in the resultant forces (both in magnitude and direction) between rigid and soft particles accumulate over time, ultimately leading to significantly diverging particle trajectories.

In the next step, we conduct a similar analysis, but with initially oblate ellipsoids ($\lambda_1 = \lambda_2$), see Fig. 16. We observe that the deviation of particle trajectories for initially oblate ellipsoidal particles is also more pronounced than for initially spherical particles, see Fig. 15. Furthermore, we find that similar to prolate ellipsoidal particles, increasing the particle aspect ratio also leads to an increased influence of particle softness on the particle trajectory for oblate ellipsoidal particles. As shown for the aspect ratio $\lambda_1 = \lambda_2 = 5$, we observe that the particles leave the cavity at the upper wall when their particle softness is $Ca \geq 0.75$, while for particles with an initial aspect ratio of $\lambda_1 = \lambda_2 = 8$ the particles already leave the cavity for $Ca \geq 0.5$. Taken together, these test cases show the importance of the presented novel approach to predict the trajectory of soft particles whose transport is significantly different from that of their rigid counterparts.

6.4. Bifurcation

Next, we inject soft particles into a simplified 3D bifurcating airway. The setup of the bifurcation study corresponds to the setup used in our previous work, see [19] and Feng and Kleinstreuer, [43]. Here, the particles are suspended in a simple bifurcation geometry corresponding to a third generation of Weibel's symmetric lung model, [44], with Reynolds number $Re = 500$, which mimics normal respiratory flow conditions in the third generation, [45]. As displayed in Fig. 17, the geometry used consists of one main and two secondary channels with a diameter $D = 6$ mm and a bifurcation angle of $\alpha = 60^\circ$.

We inject a statistically significant number of soft micro-particles, i.e. 10^5 , to investigate the influence of particle deformation on the deposition efficiency for different Stokes numbers Stk .

First, we suspend soft, initially spherical particles at the parent inlet, randomly distributed over a circular area with diameter $D_{inj} = 5.5$ mm. We assume that the particles are deposited as soon as wall contact is established (impaction and interception). In agreement with Feng and Kleinstreuer, [43], we assume that particles that are not deposited within the maximum tracking time, i.e. ten times the average residence time of the flow (see Zhang et al. [45]), leave the geometry and are not counted as deposited. Note that we employ a constant inlet velocity profile for u .

The deformable particle tracking is validated using the numerical results of Zhang et al. [45], Feng and Kleinstreuer, [43], and our previous work on inhomogeneous particles (in the homogeneous particle limit) [33] in the quasi-rigid body limit ($Ca \rightarrow 0$). Fig. 18 showcases an excellent agreement of the deposition efficiency DE with the numerical reference results [43,45] for all investigated particle Stokes numbers. Consequently, we consider the novel approach for soft, initially ellipsoidal particles as validated. The highest Stokes number considered in this study, i.e. $Stk = 0.5$, corresponds to a particle volume-equivalent diameter of $d_{eq} = 18.03$ μ m.

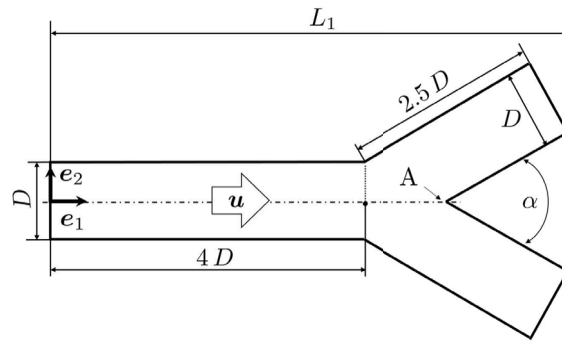


Fig. 17. Sketch of the employed simplified bifurcation model according to the third generation of Weibel’s symmetric lung model, [44]. The parent and two daughter airways are of diameter $D = 6$ mm, and the bifurcation angle is $\alpha = 60^\circ$. The gravitational direction coincides with the streamwise direction e_1 .

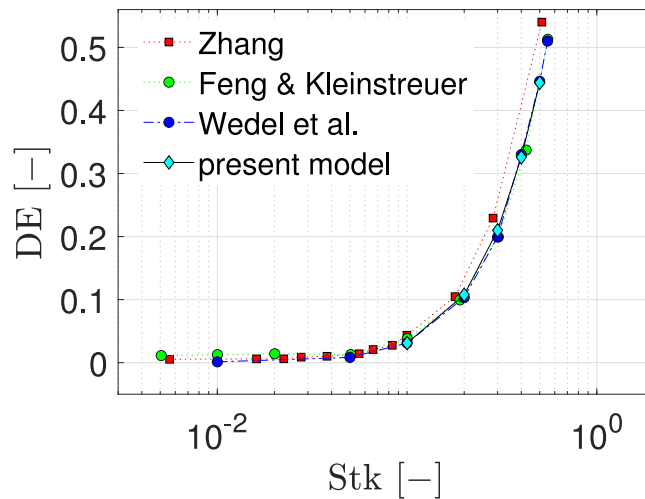


Fig. 18. Deposition efficiency $DE [-]$ in a simplified bifurcation for soft prolate ellipsoids with $\lambda = 20$ in the quasi-rigid body limit ($Ca \rightarrow 0$). The deposition efficiency is denoted as DE and defines the ratio of deposited particles to injected particles. Employed reference data: Zhang et al. [45], Feng and Kleinstreuer, [43], Wedel et al. [33].

Additionally, the maximum velocity magnitude within the bifurcation region is $U_{max} = 1.9$ m/s. Based on this information, the worst-case particle Reynolds number is estimated as $Re_p \approx 2$. Note that this estimate assumes an initial particle velocity of zero and a constant fluid velocity of U_{max} . However, in the simulations, particles are injected with the local fluid velocity, meaning that the worst-case Re_p never occurs, and in practice, $Re_p \ll 2$.

Next, we inject 10^5 particles of different initial shape, i.e. spheres ($\lambda_1^0 = \lambda_2^0 = 1$) as well as two prolate ellipsoids ($\lambda_2^0 = 1$) with either $\lambda_1^0 = 2$ or $\lambda_1^0 = 5$. Note that in the employed test case, the velocity gradient and thus the particle stretch is high mostly close to the particle walls, thus the majority of particles injected deform notably only when already reaching the near-wall region.

For initially spherical particles, see Fig. 19(a), the deviations in the deposition efficiency DE due to the particle softness are negligible. However, the deviations in DE increase towards more elongated particles, see 19(b,c). Overall, we observe a negligible to small reduction for all investigated initial particle shapes across all investigated Stk .

Next, we choose two Stokes numbers ($Stk = 0.1$ and $Stk = 0.4$) to visualize the spatial distribution of particles deposited in the simple bifurcation. The chosen Stokes numbers coincide with a volume equivalent diameter of $d_{eq} = 8.06 \mu m$ and $d_{eq} = 16.12 \mu m$, respectively. In this context, Fig. 20(a,b) visualizes the local particle deposition in the simple bifurcation for initially spherical particles as well as for prolate particles ($\lambda_1^0 = 5$) for $Stk = 0.1$ both for quasi-rigid (Left) with $\mu^s = 100000$ Pa and for soft particles (Right) with $\mu^s = 0.5$ Pa.

As displayed in Fig. 20(a,b), we observe for initially ellipsoidal particles a similar spatial deposition for $Stk = 0.1$ for both quasi-rigid (a) and soft (b) particles in the simple bifurcation. The shear modulus for the soft particle is chosen as either $\mu^s = 1$ Pa or $\mu^s = 0.5$ Pa to mimic a soft hydrogel. Furthermore, we find that for soft particles, the maximum aspect ratio in the bifurcation region is $r_{1max} = 7e-06$ m. The maximum deformation occurs near the bifurcation radius A (visualized in Fig. 17). For initially prolate ellipsoids with $\lambda_1^0 = 5$, we observe stronger elongations for particles with $Stk = 0.1$ in the region of the bifurcation radius than for the initially spherical counterpart, see Fig. 20(c,d). In addition, we also observe a compression of the particles outside the bifurcation radius, i.e. $\lambda_1 < \lambda_1^0 = 5$.

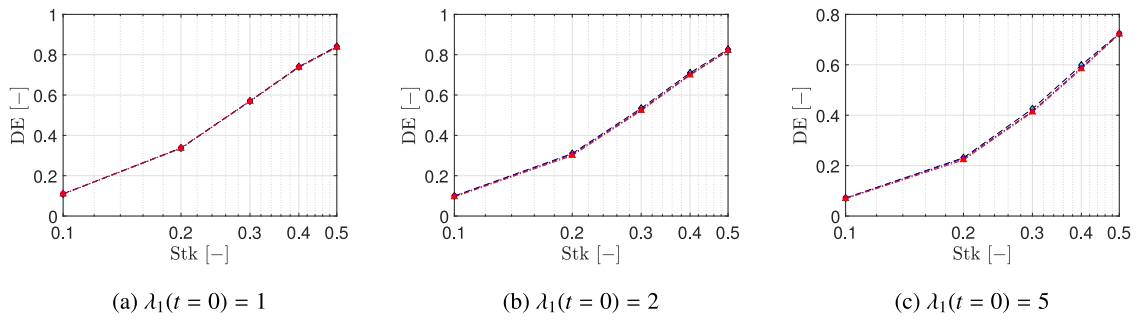


Fig. 19. Particle deposition histogram in a simple bifurcation in the streamwise direction for initial (a) spheres ($\lambda_1^0 = \lambda_2^0 = 1$) and (b) prolate ellipsoids with $\lambda_1^0 = 2$ and $\lambda_2^0 = 1$ and (c) prolate ellipsoids with $\lambda_1^0 = 5$, $\lambda_2^0 = 1$. The particle Stokes number is set to $Stk = 0.1$.

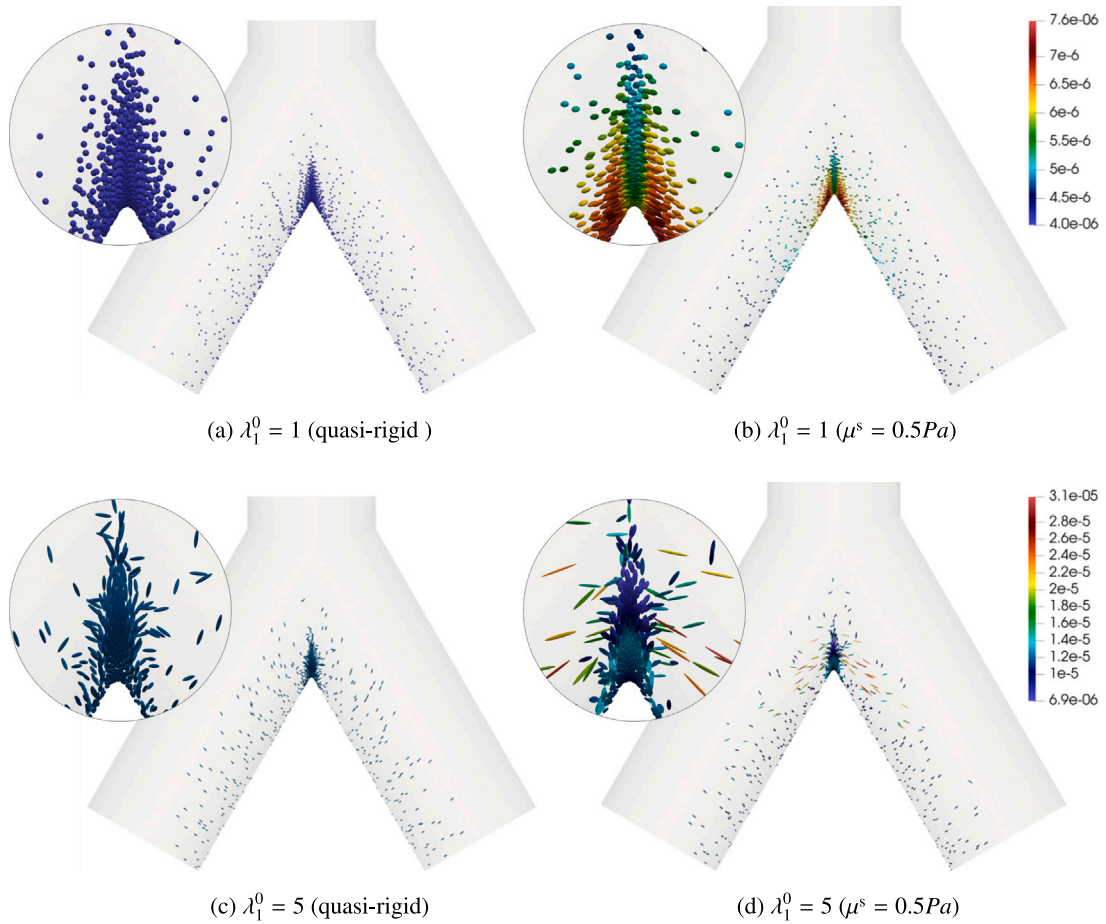


Fig. 20. Particle deposition in a simple bifurcation for initial (a,b) spheres ($\lambda_1^0 = \lambda_2^0 = 1$) and (c,d) prolate ellipsoids ($\lambda_1^0 = 5$, $\lambda_2^0 = 1$) for quasi-rigid (Left) and soft particles (Right). The particle Stokes number is set to $Stk = 0.1$. Note that the particle size is scaled for visualization purposes. The scaling factor is set to 20. The particles are colored depending on their semi-major axis r_1 .

To enable a more detailed analysis of the spatial particle deposition, we use histograms, see Fig. 21(a,b).

As highlighted in Fig. 21(a), we observe that the detailed deposition of particles along the streamwise direction changes only slightly in the case of initially spherical particles when considering quasi-rigid vs. soft particles. As shown, the deviations between the mean streamwise direction of quasi-rigid and soft particles are negligible. However, for initially prolate particles, see Fig. 21(b), we observe an increase in the deviation in spatial particle deposition when we consider quasi-rigid versus soft particles. Directly at the bifurcation radius A , we observe an increase in deposition for soft particles. Nevertheless, the general trend of the mean streamwise deposition of soft particles for $Stk = 0.1$ is slightly shifted downstream compared to the quasi-rigid counterpart.

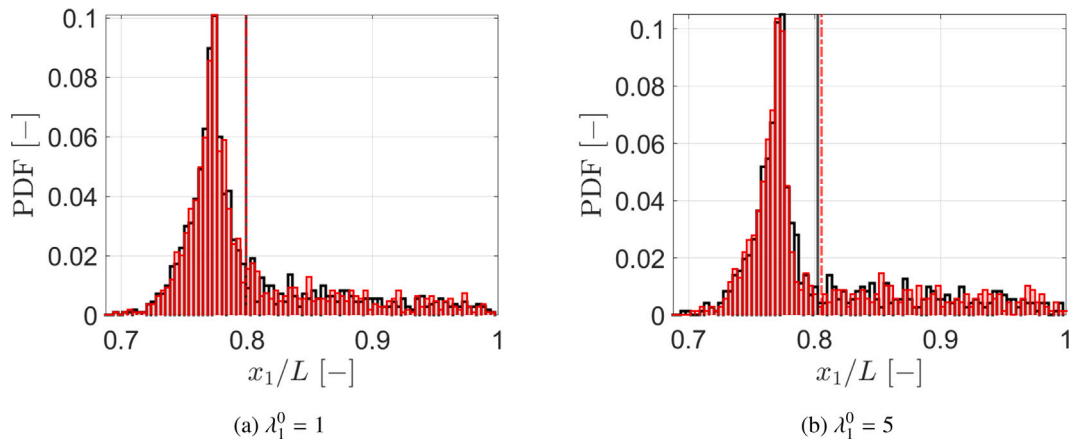


Fig. 21. Particle deposition histogram in a simple bifurcation in the streamwise direction for initial (a) spheres ($\lambda_1^0 = \lambda_2^0 = 1$) and (b) prolates ($\lambda_1^0 = 5, \lambda_2^0 = 1$). The particle Stokes number is set to $Stk = 0.1$. The total bifurcation length is $L = 0.04$ m with the bifurcation radius located at $x_1/L \approx 0.77$. Present model results for: ■ quasi-rigid particles, ■ soft particles ($G = 0.5$ Pa). Present results for: ■ quasi-rigid particles, ■ soft particles ($G = 1$ Pa), ■ soft particles ($G = 0.5$ Pa). (For interpretation of the references to color in this figure legend, the reader is referred to the web version of this article.)

Next, we visualize the local deposition of particles with $Stk = 0.4$ in the simple bifurcation, see Fig. 22(a–d). Here we compare particles with $Stk = 0.4$ of either initially spherical (a,b) or prolate (c,d) shape ($\lambda_1^0 = 5$) for both quasi-rigid (a,c) and soft particles (b,d) with $\mu^s = 0.5$ Pa.

We find that the deposition pattern in the daughter airways is altered for rigid versus soft, initially spherical particles. We also find that the highest particle stretch for soft particles occurs after the bifurcation radius. For initially prolate particles ($\lambda_1^0 = 5$), we find that the maximum stretch for soft particles does not occur directly at the bifurcation radius A , but is rather distributed over the daughter airways. At the position of the bifurcation radius, we observe a compression of the particles with ($\lambda_1 < \lambda_1^0 = 5$).

A detailed analysis of the spatial particle deposition of these particles with $Stk = 0.4$ is shown in Fig. 23(a,b). As can be seen in Fig. 23(a) for initially spherical particles, the deviation of the mean streamwise deposition location is negligible for both quasi-rigid and soft particles. However, for initially prolate particles, we observe that the deposition at the bifurcation radius A is increased for soft particles compared to quasi-rigid particles, which shifts the mean streamwise deposition of the soft particles further upstream compared to the quasi-rigid particles.

Note that the human lung consists of numerous branches. Therefore, we conjecture that the accumulation of small differences may lead to more significant variations in the overall particle trajectory, thereby enhancing the effect of particle softness on particle deposition (to be studied separately). Furthermore, this model allows for the study of particle stretch along their trajectory. Consequently, we are able to determine where a drug carrier particle breaks locally, i.e. releases the drug when it exhibits a critical stretch. Since we have demonstrated that our novel model is able to efficiently track a large number (10^5) of soft, initially ellipsoidal particles in flows, we intend to address these aspects in future work.

7. Conclusion

This work extends our recent point-particle model for soft, initially spherical particles to initially ellipsoidal particles. The model is based on Lagrangian particle tracking in combination with the point-particle approach, which allows us to simulate soft micro-particles in arbitrary flow fields. For this approach to remain valid, certain assumptions must be satisfied. These include $Re_p \ll 1$ (ensuring Stokes flow around the particle) and a dilute suspension of micro-particles (justifying the assumption of one-way coupling).

The main objective of this study is to validate and further compare the translational (barycenter) and rotation (shape) dynamics of soft, initially ellipsoidal particles with those of quasi-rigid particles. A significant achievement is the new model extension and its implementation for tracking initially non-spherical particles in arbitrary flow fields at the macro-scale. Comparisons with results from the literature validate our approach and demonstrate its ability to reproduce various findings at significantly less computational effort since no discretization of the particles is required.

To ensure the accuracy and reliability of the present model in tracking soft, initially ellipsoidal particles, we rely on both numerical and experimental studies. These include common benchmark cases such as lid-driven cavity flow, pipe flow, and a simplified bifurcation.

First, we validated the tracking code for initially ellipsoidal particles by comparing our results with the study on initially ellipsoidal particles in shear flow by Sanagavarapu et al. [21], who employed a finite element method. Our model showed excellent agreement for oblate, prolate and triaxial particles, by successfully reproducing the phase change diagram between tumbling and trembling as well as the shape dynamics at greatly reduced cost.

Next, we applied the model to prolate, soft ellipsoids in laminar pipe flow and compared our results with results for prolate, rigid ellipsoids by Tian, [37] and Cui et al. [38]. Here, our approach showed excellent agreement in the limit of a quasi-rigid body.

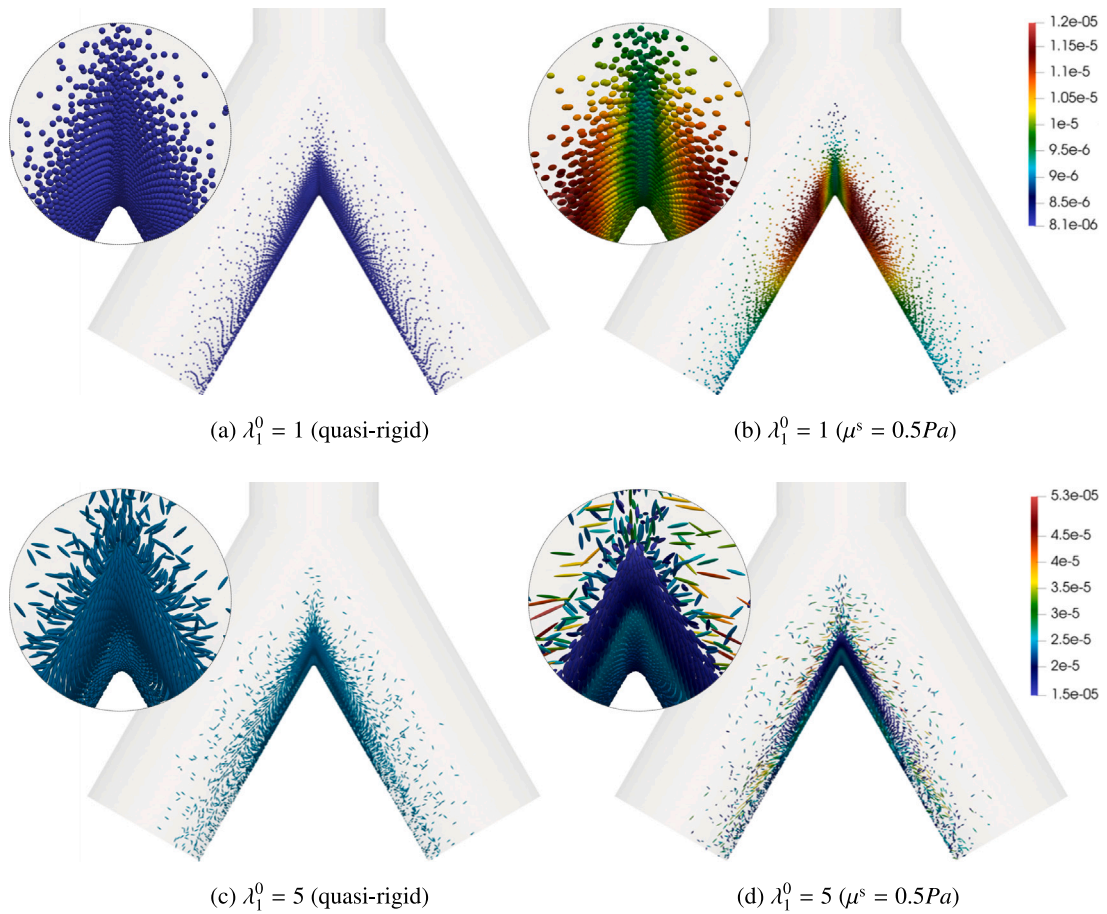


Fig. 22. Particle deposition in a simple bifurcation for initial (a) spheres ($\lambda_1 = \lambda_2 = 1$) and (b) prolates ($\lambda_1 = 5, \lambda_2 = 1$) for quasi-rigid (Left) and soft particles (Right). The particle Stokes number is set to $Stk = 0.4$. Note that the particle size is scaled for visualization purposes. The scaling factor is set to $10\times$. The particles are colored depending on their semi-major axis r_1 .

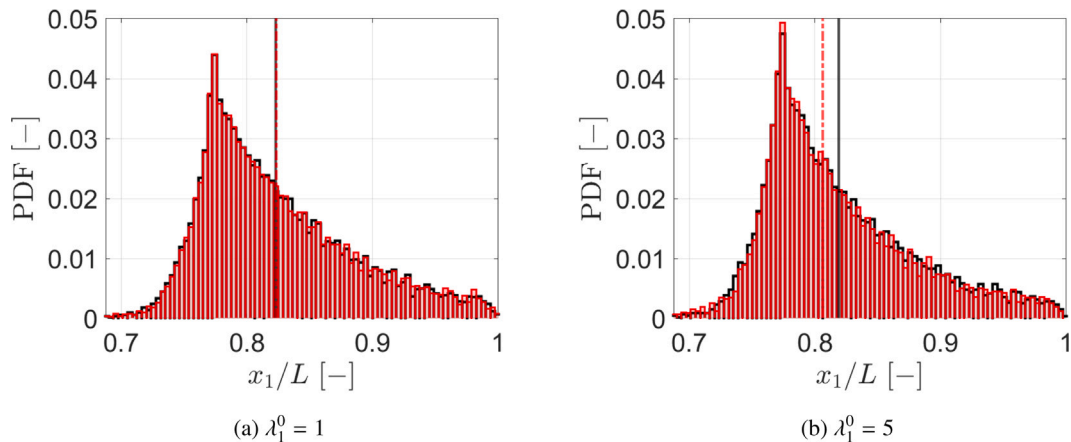


Fig. 23. Particle deposition histogram in a simple bifurcation in the streamwise direction (e_1) for initial (a) spheres ($\lambda_1^0 = \lambda_2^0 = 1$) and (b) prolates ($\lambda_1^0 = 5, \lambda_2^0 = 1$). The particle Stokes number is set to $Stk = 0.4$. The total bifurcation length is $L = 0.04$ m with the bifurcation radius located at $x_1/L \approx 0.77$. Present model results for: ■ quasi-rigid particles, ■ soft particles ($\mu^s = 0.5$ Pa). (For interpretation of the references to color in this figure legend, the reader is referred to the web version of this article.)

In addition, we observed that the softness of the particles significantly affects both the barycenter and shape dynamics, resulting in longer suspension and longer traveling distance in the streamwise direction for softer particles.

Furthermore, we studied soft particles suspended in lid-driven cavity flow. Here, we found that the deformability of the particles significantly changes the particle trajectories, especially for particles with higher initial particle aspect ratios.

Finally, we simulated the behavior of a statistically significant number (10^5) of soft particles in a simple bifurcation. Here, we observed only negligible deviations between quasi-rigid and softly deformable particles for initially spherical particles across all Stokes numbers investigated. For prolate ellipsoidal particles, however, deformability generally reduced deposition efficiency across all Stokes numbers. We conjecture that in realistic replicas of the human lung (which consists of multiple bifurcations), the deviations between soft and quasi-rigid particles is amplified. Overall, this example highlights the ability of our model to efficiently track a large number of soft particles suspended in flow.

In contrast to existing methods in the literature, which rely on costly discretizations and restrictive assumptions (e.g. incompressible and hyperelastic particles or specific flow conditions), our point-particle approach uses affine deformations and minimal degrees of freedom, making it highly efficient. Moreover, the model is applicable to arbitrary macroscopic flow fields and is not limited by specific material properties of the particles.

To summarize, our results show that particle deformability can significantly alter particle trajectories, providing a new parameter to control particle transport and deposition. Our model offers this at minimal computational cost and great versatility.

CRediT authorship contribution statement

Jana Wedel: Writing – original draft, Visualization, Validation, Software, Methodology, Investigation, Formal analysis, Data curation, Conceptualization. **Matjaž Hriberšek:** Writing – review & editing, Supervision, Resources, Project administration. **Jure Ravnik:** Writing – review & editing, Supervision, Resources, Project administration. **Paul Steinmann:** Writing – review & editing, Supervision, Resources, Project administration, Funding acquisition.

Declaration of competing interest

The authors declare that they have no known competing financial interests or personal relationships that could have appeared to influence the work reported in this paper.

Acknowledgments

The authors thank the Deutsche Forschungsgemeinschaft for the financial support in the framework of the project STE 544/75-1 and the Slovenian Research and Innovation Agency (research core funding No. P2-0196 and No. J7-60118).

Appendix. Notation

In this work, we express tensors of various orders using bold italic font. First-order tensors (vectors) are denoted by bold italic lowercase letters such as \mathbf{a} , while second-order tensors are denoted by bold italic uppercase letters such as \mathbf{A} . Using Einstein's summation convention, we can write the coordinate representation in Cartesian coordinate systems with base vectors $\mathbf{e}'_i, \mathbf{e}_i$ ($i = 1, 2, 3$) as follows:

$$\mathbf{a} = a'_i \mathbf{e}'_i = a_i \mathbf{e}_i \quad \text{and} \quad \mathbf{A} = A'_{ij} \mathbf{e}'_i \otimes \mathbf{e}'_j = A_{ij} \mathbf{e}_i \otimes \mathbf{e}_j,$$

where a'_i, a_i and A'_{ij}, A_{ij} are the corresponding coefficients in the coordinate system $\mathbf{e}'_i, \mathbf{e}_i$, respectively. The tensor coefficients a'_i, a_i and A'_{ij}, A_{ij} can be arranged in coefficient matrices, which we denote by underlined italic letters:

$$\underline{\mathbf{a}}' = \begin{bmatrix} a'_1 \\ a'_2 \\ a'_3 \end{bmatrix}, \quad \underline{\mathbf{a}} = \begin{bmatrix} a_1 \\ a_2 \\ a_3 \end{bmatrix} \quad \text{and} \quad \underline{\mathbf{A}}' = \begin{bmatrix} A'_{11} & A'_{12} & A'_{13} \\ A'_{21} & A'_{22} & A'_{23} \\ A'_{31} & A'_{32} & A'_{33} \end{bmatrix}, \quad \underline{\mathbf{A}} = \begin{bmatrix} A_{11} & A_{12} & A_{13} \\ A_{21} & A_{22} & A_{23} \\ A_{31} & A_{32} & A_{33} \end{bmatrix}.$$

Note that the employed notation is based on our previous work, [19]. The rotation matrix $\underline{\mathbf{Q}}$ transforming coefficients with respect to the base vectors \mathbf{e}_i to coefficients with respect to the base vectors \mathbf{e}'_i follows as

$$\underline{\mathbf{Q}} = \begin{bmatrix} Q_{11} & Q_{12} & Q_{13} \\ Q_{21} & Q_{22} & Q_{23} \\ Q_{31} & Q_{32} & Q_{33} \end{bmatrix} \quad \text{with} \quad Q_{ij} = \mathbf{e}'_i \cdot \mathbf{e}_j \quad \text{and} \quad \mathbf{e}'_i = Q_{ij} \mathbf{e}_j. \tag{A.1}$$

The corresponding rotation tensor $\mathbf{Q} = \mathbf{e}'_i \otimes \mathbf{e}_j$ mapping \mathbf{e}_j into $\mathbf{e}'_i = \mathbf{Q} \cdot \mathbf{e}_j$ has therefore coordinate representation $\mathbf{Q} = [\mathbf{e}'_i \cdot \mathbf{e}_j] \mathbf{e}_i \otimes \mathbf{e}_j = Q_{ji} \mathbf{e}_i \otimes \mathbf{e}_j$, i.e. the coefficient matrix of \mathbf{Q} is the matrix transpose $\underline{\mathbf{Q}}^T$. Taken together, coefficient matrices of vectors and second order tensors transform as

$$\underline{\mathbf{a}}' = \underline{\mathbf{Q}} \underline{\mathbf{a}} \quad \text{and} \quad \underline{\mathbf{A}}' = \underline{\mathbf{Q}} \underline{\mathbf{A}} \underline{\mathbf{Q}}^T. \tag{A.2}$$

Data availability

Data will be made available on request.

References

- [1] A. Podlozhnyuk, S. Pirker, C. Kloss, Efficient implementation of superquadric particles in discrete element method within an open-source framework, *Comput. Part. Mech.* 4 (2016) <http://dx.doi.org/10.1007/s40571-016-0131-6>.
- [2] Y. You, Y. Zhao, Discrete element modelling of ellipsoidal particles using super-ellipsoids and multi-spheres: A comparative study, *Powder Technol.* 331 (2018) 179–191, <http://dx.doi.org/10.1016/j.powtec.2018.03.017>.
- [3] A. Einstein, Eine neue Bestimmung der Moleküldimensionen, *Ann. Phys.* 324 (2) (1906) 289–306.
- [4] G.K. Batchelor, J.T. Green, The determination of the bulk stress in a suspension of spherical particles to order c^2 , *J. Fluid Mech.* 56 (3) (1972) 401–427, <http://dx.doi.org/10.1017/S0022112072002435>.
- [5] H. Brenner, Rheology of a dilute suspension of axisymmetric Brownian particles, *Int. J. Multiph. Flow* 1 (2) (1974) 195–341, [http://dx.doi.org/10.1016/0301-9322\(74\)90018-4](http://dx.doi.org/10.1016/0301-9322(74)90018-4).
- [6] A.B. Subramaniam, M. Abkarian, L. Mahadevan, H. Stone, Non-spherical bubbles, *Nature* 438 (2005) 209–237.
- [7] G. Jeffery, The motion of ellipsoidal particles immersed in a viscous fluid, *Proc. R. Soc. Lond. Ser. A, Contain. Pap. A Math. Phys. Character* 102 (715) (1922) 161–179, <http://dx.doi.org/10.1098/rspa.1922.0078>.
- [8] I.M. Krieger, Rheology of monodisperse latices, *Adv. Colloid Interface Sci.* 3 (2) (1972) 111–136, [http://dx.doi.org/10.1016/0001-8686\(72\)80001-0](http://dx.doi.org/10.1016/0001-8686(72)80001-0).
- [9] I. Zarraga, D. Hill, D. Jr., The characterization of the total stress of concentrated suspensions of noncolloidal spheres in Newtonian fluids, *J. Rheol.* 44 (2000) 185–220, <http://dx.doi.org/10.1122/1.551083>.
- [10] B. Snook, L.M. Davidson, J.E. Butler, O. Pouliquen, E. Guazzelli, Normal stress differences in suspensions of rigid fibres, *J. Fluid Mech.* 758 (2014) 486–507, <http://dx.doi.org/10.1017/jfm.2014.541>.
- [11] P.G. Koullapis, S.C. Kassinos, M.P. Bivolarova, A.K. Melikov, Particle deposition in a realistic geometry of the human conducting airways: Effects of inlet velocity profile, inhalation flowrate and electrostatic charge, *J. Biomech.* 49 (11) (2016) 2201–2212, <http://dx.doi.org/10.1016/j.jbiomech.2015.11.029>.
- [12] F. Lizal, M. Cabalka, M. Maly, J. Elcner, M. Belka, E.L. Sujanska, A. Farkas, P. Starha, O. Pech, O. Misik, J. Jedelsky, M. Jicha, On the behavior of inhaled fibers in a replica of the first airway bifurcation under steady flow conditions, *Aerosol Sci. Technol.* 56 (4) (2022) 367–381, <http://dx.doi.org/10.1080/02786826.2022.2027334>.
- [13] G. Bossis, J.F. Brady, Dynamic simulation of sheared suspensions. I. General method, *J. Chem. Phys.* 80 (1984) 5141–5154.
- [14] S. Gallier, E. Lemaire, L. Lobry, F. Peters, A fictitious domain approach for the simulation of dense suspensions, *J. Comput. Phys.* 256 (2014) 367–387, <http://dx.doi.org/10.1016/j.jcp.2013.09.015>.
- [15] J. Butler, B. Snook, Microstructural dynamics and rheology of suspensions of rigid fibers, *Annu. Rev. Fluid Mech.* 50 (2018) 299–318, <http://dx.doi.org/10.1146/annurev-fluid-122316-045144>.
- [16] J. Wedel, M. Štrákl, P. Steinmann, M. Hriberšek, J. Ravnik, Can CFD establish a connection to a milder COVID-19 disease in younger people? *Comput. Mech.* 67 (2021) 1497–1513, <http://dx.doi.org/10.1007/s00466-021-01988-5>.
- [17] J. Wedel, P. Steinmann, M. Štrákl, M. Hriberšek, J. Ravnik, Risk assessment of infection by airborne droplets and aerosols at different levels of cardiovascular activity, *Arch. Comput. Methods Eng.* 28 (6) (2021) 4297–4316, <http://dx.doi.org/10.1007/s11831-021-09613-7>.
- [18] J. Wedel, P. Steinmann, M. Štrákl, M. Hriberšek, Y. Cui, J. Ravnik, Anatomy matters: The role of the subject-specific respiratory tract on aerosol deposition - A CFD study, *Comput. Methods Appl. Mech. Engrg.* 401 (2022) 115372.
- [19] J. Wedel, P. Steinmann, M. Štrákl, M. Hriberšek, J. Ravnik, Shape matters: Lagrangian tracking of complex nonspherical microparticles in superellipsoidal approximation, *Int. J. Multiph. Flow* 158 (2023) 104283, <http://dx.doi.org/10.1016/j.ijmultiphaseflow.2022.104283>.
- [20] J. Ravnik, M. Štrákl, J. Wedel, P. Steinmann, M. Hriberšek, Stokes flow induced drag and torque on asbestos-like fibres can not be estimated by a simplistic ellipsoidal approximation, in: 45th International Conference on Boundary Elements and other Mesh Reduction Methods organized by WIT - Wessex Institute of Technology, U.K, 2022.
- [21] P.K. Sanagavarapu, G. Subramanian, P.R. Nott, Shape dynamics and rheology of dilute suspensions of elastic and viscoelastic particles, *J. Fluid Mech.* 949 (2022) A22, <http://dx.doi.org/10.1017/jfm.2022.704>.
- [22] I. Galaev, B. Mattiasson, *Smart Polymers: Applications in Biotechnology and Biomedicine*, vol. 20, CRC Press, 2007.
- [23] M. Villone, J. Nunes, Y. Li, H. Stone, P.L. Maffettone, Design of a microfluidic device for the measurement of the elastic modulus of deformable particles, *Soft. Matter* 15 (2019) 880–889, <http://dx.doi.org/10.1039/C8SM02272K>.
- [24] D. Silva, R. Coelho, I. Pagonabarraga, S. Succi, M. Telo da Gama, N. Araujo, Lattice Boltzmann simulation of deformable fluid-filled bodies: progress and perspectives, *Soft. Matter* 20 (2024) 2419.
- [25] H. Frohlich, R. Sack, Theory of the rheological properties of dispersions, *Proc. R. Soc. Lond.* 185 (1946) 415–430.
- [26] R. Cerf, On the frequency dependence of the viscosity of high polymer solutions, *J. Chem. Phys.* 20 (3) (1952) 395–402.
- [27] J. Goddard, C. Miller, Nonlinear effects in the rheology of dilute suspensions, *J. Fluid Mech.* 28 (1967) 657–673.
- [28] R. Roscoe, On the rheology of a suspension of viscoelastic spheres in a viscous liquid, *J. Fluid Mech.* 28 (2) (1967) 273–293, <http://dx.doi.org/10.1017/S002211206700206X>.
- [29] T. Gao, H.H. Hu, Deformation of elastic particles in viscous shear flow, *J. Comput. Phys.* 228 (6) (2009) 2132–2151, <http://dx.doi.org/10.1016/j.jcp.2008.11.029>.
- [30] T. Gao, H.H. Hu, P.P. Castañeda, Rheology of a suspension of elastic particles in a viscous shear flow, *J. Fluid Mech.* 687 (2011) 209–237, <http://dx.doi.org/10.1017/jfm.2011.347>.
- [31] T. Gao, H. Hu, P. Castañeda, Shape dynamics and rheology of soft elastic particles in a shear flow, *Phys. Rev. Lett.* 108 (2012) 058302, <http://dx.doi.org/10.1103/PhysRevLett.108.058302>.
- [32] T. Gao, H. Hu, P. Castañeda, Dynamics and rheology of elastic particles in an extensional flow, *J. Fluid. Mech.* 715 (2013) 573–596.
- [33] J. Wedel, M. Hriberšek, J. Ravnik, P. Steinmann, A novel pseudo-rigid body approach to the non-linear dynamics of soft micro-particles in dilute viscous flow, *J. Comput. Phys.* 519 (2024) 113377, <http://dx.doi.org/10.1016/j.jcp.2024.113377>.
- [34] H. Cohen, R.G. Muncaster, *The Theory of Pseudo-Rigid Bodies*, vol. 33, Springer Tracts in Natural Philosophy, 1988.
- [35] J.G. M. Kuerten, Point-particle DNS and LES of particle-laden turbulent flow - a state-of-the-art review, *Flow, Turbul. Combust.* (ISSN: 15731987) 97 (3) (2016) 689–713.
- [36] H. Brenner, The Stokes resistance of an arbitrary particle-IV arbitrary fields of flow, *Chem. Eng. Sci.* 19 (10) (1964) 703–727, [http://dx.doi.org/10.1016/0009-2509\(64\)85084-3](http://dx.doi.org/10.1016/0009-2509(64)85084-3).
- [37] L. Tian, G. Ahmadi, Z. Wang, P.K. Hopke, Transport and deposition of ellipsoidal fibers in low Reynolds number flows, *J. Aerosol Sci.* 45 (2012) 1–18, <http://dx.doi.org/10.1016/j.jaerosci.2011.09.001>.
- [38] Y. Cui, J. Ravnik, M. Hriberšek, P. Steinmann, On constitutive models for the momentum transfer to particles in fluid-dominated two-phase flows, *Adv. Struct. Mater.* 80 (2018) 1–25.
- [39] S. Tsornig, H. Capart, D. Lo, J.-S. Lai, D.-L. Young, Behaviour of macroscopic rigid spheres in lid-driven cavity flow, *Int. J. Multiph. Flow* 34 (2008) 76–101, <http://dx.doi.org/10.1016/j.ijmultiphaseflow.2007.06.007>.
- [40] J.R. Koseff, R.L. Street, The lid-driven cavity flow: A synthesis of qualitative and quantitative observations, *J. Fluids Eng.* 106 (4) (1984) 390–398, <http://dx.doi.org/10.1115/1.3243136>.

- [41] P.N. Shankar, M.D. Deshpande, Fluid mechanics in the driven cavity, *Annu. Rev. Fluid Mech.* 32 (1) (2000) 93–136, <http://dx.doi.org/10.1146/annurev.fluid.32.1.93>.
- [42] T. Chiang, W. Sheu, Numerical prediction of eddy structure in a shear-driven cavity, *Comput. Mech.* 20 (1997) 379–396, <http://dx.doi.org/10.1007/s004660050259>.
- [43] Y. Feng, C. Kleinstreuer, Analysis of non-spherical particle transport in complex internal shear flows, *Phys. Fluids* 25 (2013) 1904, <http://dx.doi.org/10.1063/1.4821812>.
- [44] E.R. Weibel, *Morphometry of the Human Lung*, Academic Press, New York, 1963.
- [45] L. Zhang, B. Asgharian, S. Anjilvel, Inertial and interceptional deposition of fibers in a bifurcating airway, *J. Aerosol Med.* 9 (3) (1996).